Available online at www.sciencedirect.com

SCIENCE DIRECT®

International Journal of Multiphase Flow

PERGAMON

International Journal of Multiphase Flow 29 (2003) 983–1015

www.elsevier.com/locate/ijmulflow

Numerical simulation of buoyant mixture flows

M.S. Nigam

BP Institute for Multiphase Flow, Madingley Rise, Madingley Road, Cambridge CB3 0EZ, UK

Received 19 May 2002; received in revised form 1 March 2003

Abstract

A 'mixture model' for the macroscopic motion of a buoyant suspension is formulated in terms of volume averaged velocities in order to ensure well-posedness of the incompressibility constraint. Conservation laws for mixture volume, momentum and the dispersed phase are complemented by a heuristic closure for the relative motion between the two phases. An efficient hybrid method for numerical simulation of mixture flows in arbitrary two-dimensional and axi-symmetric geometries is presented. The spatial discretisation is based on an *h*-type finite element method with use of a local, stabilizing upwind finite difference scheme for the advective term. Time-step and incompressibility constraints are decoupled through splitting and pressure-correction methods. The conservation equation for the dispersed phase is treated by a finite volume Roe solver with a slope limiter which ensures second-order accuracy in regions where the volume fraction is varying smoothly. Three separate applications of the code are presented to assess the validity of the various discretisation methods. The classical problem of one-dimensional batch separation is revisited and the exact analytic solution is used to evaluate the performance of the finite volume Roe solver. The results of a previous numerical simulation of spin-up from rest of a mixture are shown to be in good agreement with those produced by the current method. A numerical simulation of gravity settling underneath a curved wall (the Boycott effect) is presented for the intermediate parameter regime where both viscous and inertial effects are important. The first three terms of a Blasius series expansion for the velocity field adjacent to the curved wall are provided for comparison with the numerical results. The numerically obtained velocity profile is observed to adjust slowly to the similarity solution. In addition to verifying the global balances obtained from kinematic considerations, the simulations provide new physical insight about the interior flow-field. Notable features are the possibility of pure-fluid entrainment into the mixture region, and a stratification of the horizontal mixture–pure fluid interface due to an oscillatory vortex motion.

Keywords: Buoyant mixture; Gravity settling; Spin-up; Boycott effect; Numerical method; Finite element method

0301-9322/03/$ - see front matter
doi:10.1016/S0301-9322(03)00042-9

1. Introduction

Recent advances in super-computing have made direct numerical simulation of multi-phase flow a feasible tool for resolving complex design and calibration problems. The numerical discretisation schemes derived herein rely on the ability of a 'mixture' or 'diffusion' model to describe the macroscopic motion of a suspension. Numerous studies (Kynch, 1952; Acrivos and Herbolzheimer, 1979; Schneider, 1982; Greenspan, 1983; Greenspan and Ungarish, 1985; Schaflinger, 1997; Ungarish, 1991) have provided ample evidence that these models successfully predict the main flow characteristics of separating mixtures. Thus, any consistent discretisation based on a mixture model is expected to capture the same features while also being subjected to the limitations thereof. Amberg and Ungarish (1993) showed how existing single-phase codes may be extended to mixture flow by the inclusion of an additional equation for the volume fraction of the dispersed phase. They used finite difference methods to simulate spin-up from rest of a buoyant mixture in a circular cylinder. For simple geometries such as this one it is preferable to use regular, structured grids for which algebraic systems, amenable to solution by fast banded algorithms, are obtained. In a multitude of industrial applications, separation is more efficiently achieved in multiply connected domains enclosed by slanted or curved boundaries. This motivates the use of numerical discretisation schemes based on conforming, irregular grids with high resolution in the vicinity of corners and in boundary layers. Recently, Subia et al. (1998) used a finite element computer code to study shear-induced migration of neutrally buoyant suspensions at low to moderate Reynolds numbers. In their study, computational efficiency was not a primary consideration and the resulting algebraic systems were solved implicitly at each time-step. For separating suspensions at large Reynolds numbers, the ratio of time-scales associated with separation to those associated with the formation of viscous boundary layers can become considerable. This poses a higher demand on computational efficiency.

The object of the current study is to develop a framework for numerical computations of separating suspension flows in arbitrary multi-dimensional configurations. To achieve a high degree of geometric flexibility, the spatial discretisation is based on an h-type finite element method (Strang and Fix, 1973). This method is combined with a local finite difference scheme for the advective derivative in the momentum equation and a finite volume scheme for conservation of the dispersed phase, both of which employ the finite element grid for their implementation. Time derivatives are exclusively discretised using finite difference methods. Splitting and projection methods are used to circumvent time-step restrictions and nested iterative solves respectively. In Sections 2 and 3, the mathematical model and the numerical discretisation schemes are presented.

In Section 4, three separate applications of the code are presented to evaluate its performance. The kinematic problem of batch separation between horizontal boundaries has an exact solution which is used to assess the performance of the shock-capturing finite volume scheme for the dispersed phase. Spin-up from rest of a mixture of light particles has previously been studied by Amberg and Ungarish (1993). Both numerical and asymptotic results are found to be in good agreement with those obtained from the present simulations. In addition, the boundary layers on the horizontal plates close to the axis of rotation are essentially of the von Kármán type, which allows further comparison with asymptotic theory. While the first two examples are mainly provided to show consistency of the numerical schemes, the third application demonstrates the

geometric flexibility of the method by using different resolution in different parts of the computational domain. For gravity settling underneath a curved wall, the flow field is strongly dominated by the dynamics in a thin layer of pure fluid (the so-called Boycott layer) adjacent to the downward facing curved boundary. It is essential that this layer is adequately resolved in order to obtain useful results. A double Blasius series expansion for the flow in the Boycott layer and in the adjacent mixture region is presented. Comparisons with numerical results at a few positions along the curved wall show a relatively slow adjustment to the assumed similarity behavior. In addition to verifying the global balances obtained from kinematic considerations, the simulation also provides some new physical insight. The most notable features are the possibility of pure-fluid entrainment into the mixture region by a strong vortex localized to the top of the Boycott layer, and a stratification of the horizontal mixture–pure fluid interface resulting from the oscillations of a secondary vortex.

Although most of the qualitative results may be verified experimentally, quantitative comparisons will have to be deferred at this stage. Unfortunately, non-intrusive concentration and velocity measurements rely on rather expensive resonance imaging techniques and have so far been limited to evaluation of constitutive parameters in collision models (Phillips et al., 1992). Furthermore, current limitations on the sampling speed restrict the applicability of these methods to slowly evolving flows.

2. Formulation

Consider a mixture comprised of non-colloidal, spherical particles of radius a dispersed in a continuous fluid. Both constituents of the mixture are assumed to be incompressible. The equations will be expressed in terms of volume averaged flux densities, which in short will be referred to as velocities. In order to distinguish between volume averaged flux densities and mass averaged flux densities, the former are denoted by $\mathbf{j}$:s and the latter by $\mathbf{v}$:s. Subscripts C, d and R refer to the continuous phase, the dispersed (solid) phase and to the relative motion between the two phases. Mixture quantities are written without a subscript. All dependent variables are considered to be functions of space $\boldsymbol{x}$ and time t. The volume fraction (concentration) of particles in the mixture is represented by the variable ϕ. The density of the mixture is given by

$$\rho = \phi\rho_{\mathrm{d}} + (1-\phi)\rho_{\mathrm{C}} = (1+\varepsilon\phi)\rho_{\mathrm{C}}, \tag{1}$$

where

$$\varepsilon = \frac{\rho_{\mathrm{d}} - \rho_{\mathrm{C}}}{\rho_{\mathrm{C}}} \tag{2}$$

is the reduced density difference. The volume flux for each phase is given by

$$\mathbf{j}_{\mathrm{d}} = \phi\mathbf{v}_{\mathrm{d}}, \tag{3}$$

$$\mathbf{j}_{\mathrm{C}} = (1-\phi)\mathbf{v}_{\mathrm{C}}. \tag{4}$$

Volume averaged and mass averaged flux densities of the mixture can then be expressed as

$$\mathbf{j} = \mathbf{j}_{\mathrm{d}} + \mathbf{j}_{\mathrm{C}}, \tag{5}$$

$$\mathbf{v} = \frac{\phi\rho_{\mathrm{d}}\mathbf{v}_{\mathrm{d}} + (1-\phi)\rho_{\mathrm{C}}\mathbf{v}_{\mathrm{C}}}{\rho}. \tag{6}$$

Flow quantities describing the relative motion between the two phases are defined by the following relationships:

$$\mathbf{v}_{\mathrm{R}} = \mathbf{v}_{\mathrm{d}} - \mathbf{v}_{\mathrm{C}}, \tag{7}$$

$$\mathbf{j}_{\mathrm{R}} = \phi(1-\phi)\mathbf{v}_{\mathrm{R}}, \tag{8}$$

where $\mathbf{j}_{\mathrm{R}}$ is the 'drift flux' (see Schneider, 1982). A useful relationship between the drift flux and the particle and mixture fluxes is

$$\mathbf{j}_{\mathrm{d}} = \mathbf{j}_{\mathrm{R}} + \phi\mathbf{j}. \tag{9}$$

The hydrodynamics of the mixture are described by a set of conservation laws for mixture momentum and for each phase. These are complemented by a heuristic closure for the drift flux. Conservation of the dispersed and continuous phases is expressed by

$$\frac{\partial\phi}{\partial t} + \nabla\cdot\mathbf{j}_{\mathrm{d}} = 0, \tag{10}$$

$$\frac{\partial(1-\phi)}{\partial t} + \nabla\cdot\mathbf{j}_{\mathrm{C}} = 0. \tag{11}$$

Adding Eqs. (10) and (11) gives an expression for the conservation of mixture volume:

$$\nabla\cdot(\mathbf{j}_{\mathrm{d}} + \mathbf{j}_{\mathrm{C}}) = 0 \Rightarrow \nabla\cdot\mathbf{j} = 0. \tag{12}$$

On averaging the rate of change of momentum of both phases (see Appendix A) and simplifying the result using the previously stated kinematic relationships, the following momentum equation is obtained:

$$\frac{\partial}{\partial t}(\mathbf{j} + \varepsilon\mathbf{j}_{\mathrm{d}}) + \nabla\cdot\left[\mathbf{j}\mathbf{j} + \frac{\mathbf{j}_{\mathrm{R}}\mathbf{j}_{\mathrm{R}}}{\phi(1-\phi)} + \frac{\varepsilon\mathbf{j}_{\mathrm{d}}\mathbf{j}_{\mathrm{d}}}{\phi}\right] = \frac{1}{\rho_{\mathrm{C}}}\nabla\cdot\underline{\underline{\Sigma}} + (1+\varepsilon\phi)\mathbf{f}. \tag{13}$$

In Eq. (13), $\mathbf{f}$ is the body force which henceforth will be assumed to be conservative. A generalized Newtonian relationship is specified for the stress tensor:

$$\underline{\underline{\Sigma}} = -P\underline{\underline{I}} + \eta_0\eta(\phi)[\nabla\mathbf{j} + (\nabla\mathbf{j})^{\mathrm{T}}]. \tag{14}$$

Here, P is the pressure, $\eta(\phi)$ is the effective suspension viscosity and η_0 is the dynamic viscosity of the suspending fluid. The expression used here for the effective viscosity is a semi-empirical correlation of the type suggested by Krieger (1972),

$$\eta(\phi) = \left(1 - \frac{\phi}{\phi_{\mathrm{M}}}\right)^{-K\phi_{\mathrm{M}}}, \tag{15}$$

where ϕ_{M} is the maximum packing, taken to be 0.68 and $K = 2.5$. While expressions (14) and (15) are unable to capture the detailed dynamics of the sediment regions, they give good estimates of where in the computational domain sediments will be deposited. Rearranging the terms in Eq. (13) and introducing the reduced pressure, p, for a conservative body force, leads to

$$\frac{\partial \mathbf{j}}{\partial t} + \mathbf{j}\cdot\nabla\mathbf{j} = -\frac{1}{\rho_C}\nabla p + v_0\nabla\cdot[\eta(\phi)(\nabla\mathbf{j} + (\nabla\mathbf{j})^T)] - \nabla\cdot\left[\frac{\mathbf{j}_R\mathbf{j}_R}{\phi(1-\phi)}\right] - \varepsilon\left[\frac{\partial \mathbf{j}_d}{\partial t} + \nabla\cdot\left(\frac{\mathbf{j}_d\mathbf{j}_d}{\phi}\right) - \phi\mathbf{f}\right]. \tag{16}$$

Hence, the relative density difference induces a forcing, proportional to the effective acceleration of the dispersed phase. A closure for the drift flux is given by:

$$\mathbf{j}_R = -\frac{2\varepsilon a^2}{9v_0}\frac{\phi(1-\phi)^2}{\eta(\phi)}\left[\frac{\partial \mathbf{j}}{\partial t} + \mathbf{j}\cdot\nabla\mathbf{j} - \mathbf{f}\right], \tag{17}$$

which is valid for non-interacting particles in quasi-steady creeping motion relative to the fluid. For a more detailed discussion on this type of closures, see Ungarish (1993). Additional terms, accounting for shear-induced particle migration (Phillips et al., 1992), may be added to expression (17). For gravity induced phase separation, the ratio of the buoyancy flux to the migration flux scales as $\varepsilon gL/(v_0\dot{\gamma})$, where $\dot{\gamma}$ is the local shear-rate and L is the characteristic length-scale of the flow field. In what follows, this ratio is assumed to be small such that shear-induced migration is negligible compared to the buoyancy flux. The standard no-flux and no-slip conditions are imposed on the mixture velocity $\mathbf{j}$. The latter of these is obviously an approximation since particles may slide or roll along a solid boundary. A macroscopic model for the apparent wall slip velocity has been suggested by Jana et al. (1995). The slip velocity was shown to be given by $U_s = \beta(\phi)a\dot{\gamma}$, where $\beta(\phi)$ becomes large as ϕ approaches maximum packing and vanishes for $\phi < 0.4$. Thus, in spite of the small values of a, U_s may reach appreciable levels at high particle concentrations. At such levels, however, the approximations (14) and (15) do not warrant the additional level of complexity involved in attempting to isolate the effects of wall slip in the numerical simulations. Inflow conditions are specified for the particle flux $\mathbf{j}_d$ when applicable, and on solid boundaries, the normal component of the particle flux is set equal to zero. Eq. (12) is the reason why $\mathbf{j}$ was chosen over $\mathbf{v}$ as the principal variable in the momentum equation. The numerical treatment of the incompressibility constraint is facilitated if the no-flux condition is imposed on $\mathbf{j}$ instead of on $\mathbf{v}$. Solutions to Eq. (10) involve kinematic shocks representing interfaces between pure fluid, mixture and sediment. In addition to the aforementioned boundary conditions, shock-conditions given in Appendix A must also be satisfied. While the preceding model does not give a complete description of suspension flows in general, it will be shown to capture the fundamental features of buoyancy driven phase separation.

3. Numerical discretisation

For the purpose of describing the numerical methods, the following form of the mixture-model equations will be considered:

$$\frac{\partial \mathbf{j}}{\partial t} + \mathbf{j}\cdot\nabla\mathbf{j} = -\frac{1}{\rho_C}\nabla p + v_0\nabla\cdot[\eta(\phi)(\nabla\mathbf{j} + (\nabla\mathbf{j})^T)] + \mathbf{F}, \tag{18}$$

$$\nabla\cdot\mathbf{j} = 0, \tag{19}$$

$$\frac{\partial \phi}{\partial t} + \nabla \cdot \mathbf{j}_{\mathrm{d}} = 0, \tag{20}$$

$$\mathbf{j}_{\mathrm{R}} = -\frac{2\varepsilon a^2}{9 v_0} \frac{\phi(1-\phi)^2}{\eta(\phi)} \left[\frac{\partial \mathbf{j}}{\partial t} + \mathbf{j} \cdot \nabla \mathbf{j} - \mathbf{f} \right], \tag{21}$$

$$\mathbf{j}_{\mathrm{d}} = \mathbf{j}_{\mathrm{R}} + \phi \mathbf{j}. \tag{22}$$

Here, $\mathbf{F}$ represents the extra stress due to the relative motion and the forcing induced by the density difference between the two phases. a is the particle radius and g is the constant of gravity. The equations are solved in a region $\mathscr{R}$ with boundary $\partial\mathscr{R}$ for times $0 \leqslant t \leqslant T$. The mixed initial/boundary value problem defined in (18)–(22) is treated by a method of lines approach, which separates the spatial and temporal discretisations. The temporal discretisations are exclusively accomplished by finite difference methods while the spatial discretisations use a combination of finite elements, finite differences and finite volumes. Eqs. (18) and (19) resemble a Navier–Stokes system, and the numerical solution procedure for such is governed by standard methods which will only be briefly outlined in this section. The attention will instead be focused on the advection problem for the dispersed phase, Eqs. (20)–(22).

3.1. Temporal discretisation of the momentum equation

The viscous term in (18) is treated implicitly to avoid unnecessarily severe restrictions on the time-step. Hence, the time-step is restricted by a CFL-type (Courant et al., 1967) condition due to the explicit treatment of the non-linear term. An operator-integration-factor technique by Maday et al. (1990) is used to split problem (18) and (19) into an advective part and a Stokes part. The motivation for this is to decouple the CFL-limited advection steps from the Stokes solver. This way a larger time-step may be used for the computationally expensive Stokes problem. For second-order backwards differentiation, the OIF splitting yields the following subproblems:

$$\frac{3}{2\Delta t}\mathbf{j}^n - v_0 \nabla \cdot [\eta(\phi^n)(\nabla \mathbf{j}^n + (\nabla \mathbf{j}^n)^{\mathrm{T}})] + \frac{1}{\rho_{\mathrm{C}}} \nabla p^n = \frac{2}{\Delta t}\tilde{\mathbf{j}}_1^n - \frac{1}{2\Delta t}\tilde{\mathbf{j}}_2^n + \mathbf{F}^n, \tag{23}$$

$$\nabla \cdot \mathbf{j}^n = 0, \tag{24}$$

where $\tilde{\mathbf{j}}_i^n \equiv \tilde{\mathbf{j}}_i(\boldsymbol{x}, t^n)$ are obtained from the pure advection problem

$$\frac{\partial \tilde{\mathbf{j}}_i}{\partial t} + \mathbf{j} \cdot \nabla \tilde{\mathbf{j}}_i = \mathbf{0}, \tag{25}$$

$$\tilde{\mathbf{j}}_i(\boldsymbol{x}, t^{n-i}) = \mathbf{j}(\boldsymbol{x}, t^{n-i}). \tag{26}$$

The temporal discretisation of problem (25) and (26) is accomplished by a fourth-order Runge–Kutta scheme with a time-step which satisfies the CFL condition. The values of $\mathbf{j}$ needed in the Runge–Kutta evaluations of (25) are interpolated from the velocity fields at previous time-steps, $(\mathbf{j}^{n-1}, \mathbf{j}^{n-2}, \mathbf{j}^{n-3})$, (see Appendix B). Interpolation is also used in evaluating the terms comprising $\mathbf{F}^n$ in Eq. (23). The accuracy of the combined problem (23), (24) and (25), (26) is $\mathrm{O}(\Delta t^2)$. In addition to the temporal OIF splitting, the incompressibility constraint in the Stokes problem is decoupled through an $\mathrm{O}(\Delta t^2)$ pressure-correction method:

$$\frac{3}{2\Delta t}\mathbf{j}^* - v_0\nabla\cdot[\eta(\phi^n)(\nabla\mathbf{j}^* + (\nabla\mathbf{j}^*)^{\mathrm{T}})] = -\frac{1}{\rho_{\mathrm{C}}}\nabla p^{n-1} + \mathbf{f}^n, \tag{27}$$

$$\mathbf{j}^n = \mathbf{j}^* - \frac{2\Delta t}{3\rho_{\mathrm{C}}}\nabla\delta p, \tag{28}$$

$$\nabla\cdot\mathbf{j}^n = 0, \tag{29}$$

$$p^n = p^{n-1} + \delta p, \tag{30}$$

where $\mathbf{f}^n$ includes all terms on the right-hand side of Eq. (23). $\mathbf{j}^*$ is chosen to satisfy the same boundary conditions as $\mathbf{j}^n$, which is consistent for Dirichlet conditions.

3.2. Spatial discretisation of the momentum equation

The particular class of problems of interest here is multi-dimensional incompressible flow problems in arbitrary geometries with expected irregularities in some of the dependent variables. These irregularities are due to discontinuities associated with interfaces between pure fluid, mixture and sediment. A Galerkin finite element method was chosen for the spatial discretisation of Eqs. (23) and (24). In addition to being able to discretise arbitrarily complex configurations, it provides easy use of unstructured grids with enhanced resolution in regions with large gradients. It also allows for a natural extension to adaptive methods. The Stokes problem is recast in an equivalent variational form, $(\mathbf{j}^n, p^n) \in (X^{\mathrm{v}}, X^{\mathrm{p}})$, from which a finite element discretisation is achieved by restricting $\mathbf{j}^n$ and p^n to conforming finite-dimensional subspaces $(\mathbf{j}_h^n, p_h^n) \in (X_h^{\mathrm{v}}, X_h^{\mathrm{p}})$, where $X_h^{\mathrm{v}} \subset X^{\mathrm{v}}$ and $X_h^{\mathrm{p}} \subset X^{\mathrm{p}}$. Before stating the variational problem, $\mathbf{j}_h^n$ is divided into two parts: $\mathbf{j}_h^n = \mathbf{j}_{h0}^n + \mathbf{j}_{h\mathrm{b}}^n$, where $\mathbf{j}_{h0}^n = \mathbf{0}$ on $\partial\mathscr{R}$ and $\mathbf{j}_{h\mathrm{b}}^n$ is the prescribed boundary condition. The variational equivalent of Eqs. (27)–(30) is given below.

Find $\mathbf{j}_{h0}^n \in X_{h0}^{\mathrm{v}}$ and $p_h^n \in X_h^{\mathrm{p}}$ such that:

$$\frac{3}{2\Delta t}(\mathbf{j}_{h0}^*, \mathbf{v}) + v_0(\eta(\phi_h^n)[\nabla\mathbf{j}_{h0}^* + (\nabla\mathbf{j}_{h0}^*)^{\mathrm{T}}], \nabla\mathbf{v}) = \frac{1}{\rho_{\mathrm{C}}}(p_h^{n-1}, \nabla\cdot\mathbf{v}) + (\mathbf{f}_{h\mathrm{b}}^n, \mathbf{v}), \tag{31}$$

$$\frac{2\Delta t}{3\rho_{\mathrm{C}}}(\nabla q, \nabla\delta p_h) = (q, \nabla\cdot\mathbf{j}_{h0}^n) - (q, \nabla\cdot\mathbf{j}_{h0}^*), \tag{32}$$

$$-(q, \nabla\cdot\mathbf{j}_{h0}^n) = (q, \nabla\cdot\mathbf{j}_{h\mathrm{b}}^n), \tag{33}$$

$$(\mathbf{j}_{h0}^n, \mathbf{v}) = (\mathbf{j}_{h0}^*, \mathbf{v}) + \frac{2\Delta t}{3\rho_{\mathrm{C}}}(\delta p_h, \nabla\cdot\mathbf{v}), \tag{34}$$

$$p_h^n = p_h^{n-1} + \delta p_h, \tag{35}$$

$\forall\mathbf{v} \in X_{h0}^{\mathrm{v}}$ and $\forall q \in X_h^{\mathrm{p}}$.

X_{h0}^{v} is the finite-dimensional velocity subspace restricted to homogeneous Dirichlet conditions. Eq. (32) was obtained by multiplying Eq. (28) through by the gradient of the test function q and integrating the first term on each side of the equation by parts. The boundary integrals cancel since $\mathbf{j}_{h\mathrm{b}}^* = \mathbf{j}_{h\mathrm{b}}^n$. The linear terms in $\mathbf{f}_{h\mathrm{b}}^n$ which now includes the boundary forcing are restricted to

the subspace X_h^{v} together with ϕ_h^n. The non-linear stresses, induced by the density difference and the relative motion between the two phases respectively, are treated by a group finite element approach (Fletcher, 1983). Hence, the expression:

$$\frac{\mathbf{j}_{\mathrm{R}}\mathbf{j}_{\mathrm{R}}}{\phi(1-\phi)}+\frac{\varepsilon\mathbf{j}_{\mathrm{d}}\mathbf{j}_{\mathrm{d}}}{\phi} \tag{36}$$

is evaluated nodally and projected onto the subspace X_h^{v}. Since $\mathbf{j}_{h0}^n$ and $\mathbf{v}$ belong to the same subspace, the method is of the Galerkin type. The inner product in (31)–(35) is defined for all square integrable functions in $\mathscr{R}$ as

$$\forall\varphi,\psi\in\mathscr{L}^2(\mathscr{R}):\quad (\varphi,\psi)=\int_{\mathscr{R}}\varphi(\boldsymbol{x})\psi(\boldsymbol{x})\,\mathrm{d}\boldsymbol{x}, \tag{37}$$

where the integrals are evaluated using Gauss quadrature (see Strang and Fix, 1973). Triangular elements with first-order tensor-product polynomials were used for both velocity and pressure, yielding a discretisation error of $\mathrm{O}(h^2)$ in terms of the $\mathscr{L}^2$-norm, where h is the grid parameter. Spurious pressure modes, excited by discretisations with equal order tensor-product polynomials for velocity and pressure, are successfully suppressed through the introduction of Eq. (32). Hence, divergence stabilization is here obtained by inverting a discrete Laplacian to find the pressure increment. The discrete linear system corresponding to (31)–(35) is given in Appendix C.

For the spatial discretisation of the advective term in (25), a third-order accurate upwind, finite difference formula of the type proposed by Tabata and Fujima (1991) has been implemented. At each grid point $\boldsymbol{x}_i$, the advective derivative is discretised along the direction of the local velocity vector using three additional points, one downwind and two upwind. The additional discretisation points were chosen to be the points at which a straight line, parallel to the nodal velocity vector, crosses element boundaries (Fig. 1). The finite difference discretisation is based on the following expansion of the advective derivative for a scalar function $\varphi(\boldsymbol{x})$:

$$\begin{aligned}\mathbf{j}\cdot\nabla\varphi]_{\boldsymbol{x}=\boldsymbol{x}_i}=|\mathbf{j}(\boldsymbol{x}_i)|\Bigg[&c_1\varphi\left(\boldsymbol{x}_i+h_1\frac{\mathbf{j}(\boldsymbol{x}_i)}{|\mathbf{j}(\boldsymbol{x}_i)|}\right)+c_0\varphi(\boldsymbol{x}_i)\\&+c_2\varphi\left(\boldsymbol{x}_i-h_2\frac{\mathbf{j}(\boldsymbol{x}_i)}{|\mathbf{j}(\boldsymbol{x}_i)|}\right)+c_3\varphi\left(\boldsymbol{x}_i-h_3\frac{\mathbf{j}(\boldsymbol{x}_i)}{|\mathbf{j}(\boldsymbol{x}_i)|}\right)\Bigg]+\mathrm{O}(\max(h_i^3)).\end{aligned} \tag{38}$$

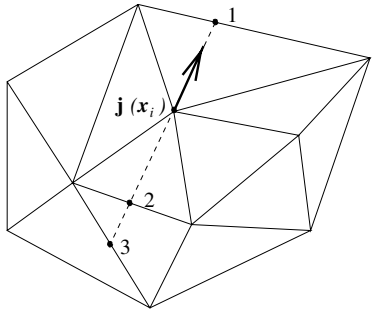

Fig. 1. Finite difference discretisation points for advection of momentum.

Here h_l, $l = 1,2,3$ is the distance from $\boldsymbol{x}_i$ to discretisation point l and the coefficients c_l, $l = 0,1,2,3$ are given by

$$\begin{aligned} c_1 &= \frac{h_2 h_3}{h_1(h_1+h_2)(h_1+h_3)}, \\ c_2 &= -\frac{h_1 h_3}{h_2(h_1+h_2)(h_3-h_2)}, \\ c_3 &= \frac{h_1 h_2}{h_3(h_1+h_3)(h_3-h_2)}, \\ c_0 &= -c_1 - c_2 - c_3. \end{aligned} \tag{39}$$

The values of $\varphi(\boldsymbol{x}_i)$ at the discretisation points are computed from the finite element basis functions. The spatial discretisation of problem (25) and (26) is readily obtained from (38) and (39) by substituting the components of $\tilde{\mathbf{j}}_1$ and $\tilde{\mathbf{j}}_2$ for φ. Upwinding stabilizes the scheme in the sense that it allows for a larger cell Peclet number (in terms of the Reynolds number $Re = UL/v_0$ and the grid parameter h, $Pe = hRe$) to be used in the simulations.

3.3. Numerical discretisation of the advection equation for the dispersed phase

This section is concerned with the pure advection problem (20)–(22) and the numerical treatment of the associated discontinuities. The approach, taken here, is of the 'shock-capturing' type and adds a small amount of diffusion to stabilize the numerical method. Hence, the discontinuities will be represented by thin but finite transition regions rather than sharp jumps. The simplest way of accomplishing this is to use first-order upwinding, which introduces an $O(h)$ diffusive error term. In order to limit this error to regions where it is necessary for numerical stability, a slope-limiting scheme is applied. On regular grids, these methods have been shown to give a substantial improvement over first-order upwinding methods (LeVeque, 1990). For irregular grids, the application of slope limiters becomes more complicated. Löhner (1988) developed a flux-corrected-transport scheme in the finite element context. However, as will be shown in the next section, because the limiting procedure does not take into account the direction of wave-propagation, it may sometimes produce solutions which do not comply with the proper entropy condition. For the problem considered here, a finite volume scheme was developed. In addition to being conservative, the finite volume method is easy to use with the already supplied finite element mesh, and the finite element basis functions provide a natural tool for the reconstructions which are necessary for the higher-order correction. The average value $\bar{\phi}^k$, on each element $\mathscr{R}^k$, is used to evaluate local fluxes $\mathbf{j}_{\mathrm{d}}^{k,i}$ from (21) and (22) for each vertex i of the element,

$$\mathbf{j}_{\mathrm{d}}^{k,i} = -\frac{2\varepsilon a^2}{9v_0}\frac{\bar{\phi}^k(1-\bar{\phi}^k)^2}{\eta(\bar{\phi}^k)}\left[\frac{\partial \mathbf{j}_i}{\partial t} + (\mathbf{j}\cdot\nabla\mathbf{j})_i - \mathbf{f}_i\right] + \bar{\phi}^k\mathbf{j}_i, \tag{40}$$

where the advection term is evaluated from the previously described four-point finite difference formula and the time derivative is obtained from a second-order backwards differentiation scheme (see Appendix B). The elemental fluxes $\mathbf{j}_{\mathrm{d}}^k(\boldsymbol{x},t)$ are thus represented by first-order tensor-product polynomials which are discontinuous across element boundaries $\partial\mathscr{R}^k$,

$$\mathbf{j}_{\mathrm{d}}^{k}(\boldsymbol{x},t)=\sum_{i=1}^{3}\mathbf{j}_{\mathrm{d}}^{k,i}(t)\varphi^{k,i}(\boldsymbol{x}), \tag{41}$$

where $\varphi^{k,i}(\boldsymbol{x})$ is the finite element basis function on element $\mathscr{R}^k$ corresponding to vertex i. Next, a low order estimate of $\bar{\phi}^k$ at $t+\Delta t/2$ is obtained by integrating Eq. (20) over each element:

$$\bar{\phi}^{k}(t+\Delta t/2)=\bar{\phi}^{k}(t)-\frac{\Delta t}{2V_{\mathscr{R}^k}}\oint_{\partial\mathscr{R}^k}\mathbf{j}_{\mathrm{d}}^{k}(\boldsymbol{x},t)\cdot\hat{\boldsymbol{n}}\,\mathrm{d}S, \tag{42}$$

where $V_{\mathscr{R}^k}$ and $\partial\mathscr{R}^k$ are the volume and surface of the element, and $\hat{\boldsymbol{n}}$ is the outward surface normal. The fluxes $\mathbf{j}_{\mathrm{d}}^{k}(\boldsymbol{x},t)$ are replaced by upwind fluxes where the upwind directions are given by the directions of propagation of the jump discontinuities across element boundaries. Using the notation of Fig. 2, the upwind flux at vertex i is given by

$$\mathbf{j}_{\mathrm{d}}^{\mathrm{upwind},i}\cdot\hat{\boldsymbol{n}}=\mathbf{j}_{\mathrm{d}}^{l,i}\cdot\hat{\boldsymbol{n}}+\mathbf{H}\left(\frac{\hat{\boldsymbol{n}}\cdot(\mathbf{j}_{\mathrm{d}}^{l,i}-\mathbf{j}_{\mathrm{d}}^{k,i})}{\bar{\phi}^{l}-\bar{\phi}^{k}}\right)(\mathbf{j}_{\mathrm{d}}^{k,i}-\mathbf{j}_{\mathrm{d}}^{l,i})\cdot\hat{\boldsymbol{n}}, \tag{43}$$

where $\mathbf{H}$ is the Heaviside function. Since $\mathbf{j}_{\mathrm{d}}^{\mathrm{upwind}}(\boldsymbol{x},t)$ is represented by the local finite element basis functions, which are first-order polynomials along each elemental boundary segment, the surface integrals are easily evaluated analytically. Second-order accuracy is here obtained by a MUSCL-type method. The low order solution $\bar{\phi}^k(t+\Delta t/2)$ is used to estimate the gradients of ϕ at $t+\Delta t/2$. First, ϕ is reconstructed using the finite element interpolation functions,

$$\phi_m=\mathbf{M}_{\mathbf{L}_{mm}}^{-1}\sum_{k}\mathbf{I}_{mk}\bar{\phi}^{k}, \tag{44}$$

where

$$\mathbf{I}_{mk}=\int_{V_{\mathscr{R}^k}}\varphi_m(\boldsymbol{x})\,\mathrm{d}V. \tag{45}$$

$\varphi_m(\boldsymbol{x})$ is now the finite element basis function associated with the global node m and $\mathbf{M}_{\mathbf{L}}$ is the lumped finite element mass matrix. Next, the average of the derivative of ϕ with respect to x_p on element $\mathscr{R}^k$ is given by

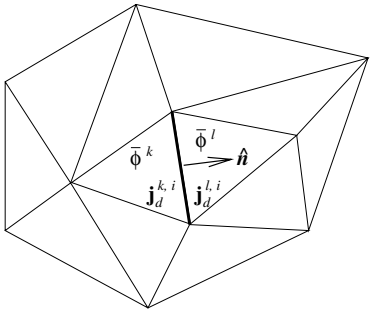

Fig. 2. Evaluation of upwind fluxes.

$$\left(\frac{\partial\phi}{\partial x_p}\right)^k = \frac{1}{V_{\mathscr{R}^k}}\int_{V_{\mathscr{R}^k}} \sum_m \phi_m \frac{\partial\varphi_m}{\partial x_p}\,\mathrm{d}V. \tag{46}$$

This yields a second-order reconstruction at the intermediate time level $t+\Delta t/2$,

$$\phi^{k,i} = \bar{\phi}^k + \sum_p \theta_p^k \left(\frac{\partial\phi}{\partial x_p}\right)^k \left(x_p^{k,i} - x_{\mathrm{C}p}^k\right), \tag{47}$$

where $x_p^{k,i}$ is the value of coordinate x_p at vertex i of element $\mathscr{R}^k$ and $x_{\mathrm{C}p}^k$ is the value of x_p at the center of the element. θ_p^k are slope limiters which are applied to enforce monotonicity. The limiting procedure is equivalent to that of Peyrard and Villedieu (1998) except that separate limiters are used for each coordinate direction,

$$\theta_p^k = \min(1, \theta_p^{\max}, \theta_p^{\min}), \tag{48}$$

$$\theta_p^{\max} = \frac{\bar{\phi}^{\max} - \bar{\phi}^q}{\Delta_p^{\max}}, \tag{49}$$

$$\theta_p^{\min} = \frac{\bar{\phi}^q - \bar{\phi}^{\min}}{\Delta_p^{\min}}, \tag{50}$$

where $\bar{\phi}^{\max}$ and $\bar{\phi}^{\min}$ are the maximum/minimum values of the elements neighboring the boundary segments of $\mathscr{R}^k$. $\bar{\phi}^q$ is given by $\bar{\phi}^q = \max(\bar{\phi}^{\min}, \min(\bar{\phi}^k, \bar{\phi}^{\max}))$ and

$$\Delta_p^{\max} = \left|\max_i \left\{\left(\frac{\partial\phi}{\partial x_p}\right)^k (x_p^{k,i} - x_{\mathrm{C}p}^k)\right\}\right|, \tag{51}$$

$$\Delta_p^{\min} = \left|\min_i \left\{\left(\frac{\partial\phi}{\partial x_p}\right)^k (x_p^{k,i} - x_{\mathrm{C}p}^k)\right\}\right|. \tag{52}$$

Hence, the second-order update of $\bar{\phi}^k$ at time $t+\Delta t$ is given by,

$$\bar{\phi}^k(t+\Delta t) = \bar{\phi}^k(t) - \frac{\Delta t}{V_{\mathscr{R}^k}} \oint_{\partial\mathscr{R}^k} \mathbf{j}_{\mathrm{d}}^k(\boldsymbol{x}, t+\Delta t/2)\cdot\hat{\boldsymbol{n}}\,\mathrm{d}S, \tag{53}$$

$$\mathbf{j}_{\mathrm{d}}^k(\boldsymbol{x}, t+\Delta t/2) = \sum_{i=1}^{3} \mathbf{j}_{\mathrm{d}}^{\mathrm{upwind},i}(t+\Delta t/2)\varphi^{k,i}(\boldsymbol{x}), \tag{54}$$

$$\mathbf{j}_{\mathrm{d}}^{\mathrm{upwind},i}\cdot\hat{\boldsymbol{n}} = \mathbf{j}_{\mathrm{d}}^{l,i}\cdot\hat{\boldsymbol{n}} + \mathbf{H}\left(\frac{\hat{\boldsymbol{n}}\cdot(\mathbf{j}_{\mathrm{d}}^{l,i} - \mathbf{j}_{\mathrm{d}}^{k,i})}{\phi^{l,i} - \phi^{k,i}}\right)(\mathbf{j}_{\mathrm{d}}^{k,i} - \mathbf{j}_{\mathrm{d}}^{l,i})\cdot\hat{\boldsymbol{n}}, \tag{55}$$

$$\mathbf{j}_{\mathrm{d}}^{k,i} = -\frac{2\varepsilon a^2}{9v_0}\frac{\phi^{k,i}(1-\phi^{k,i})^2}{\eta(\phi^{k,i})}\left[\frac{\partial\mathbf{j}_i}{\partial t} + (\mathbf{j}\cdot\nabla\mathbf{j})_i - \mathbf{f}_i\right] + \phi^{k,i}\mathbf{j}_i, \tag{56}$$

where (56) is evaluated at $t+\Delta t/2$ and $\phi^{k,i}$ is obtained from (47). Once $\bar{\phi}^k$ at time t^n has been updated, the nodal values of ϕ^n to be used in the finite element discretisation of the momentum equation are readily obtained from (44) and (45).

Each time-step, n, in the numerical implementation is initiated by updating the volume fraction ϕ^n. This is followed by the pure advection problem for $\tilde{\mathbf{j}}_1^n$ and $\tilde{\mathbf{j}}_2^n$. Due to the explicit treatment of these subproblems, only diagonal solvers are needed in the Runge–Kutta evaluations. Finally, the Stokes problem is solved using the conjugate gradient method preconditioned by incomplete Cholesky factorizations.

4. Applications to buoyant suspension flows

In this section, three separate applications of the code are provided. The first application treats the one-dimensional settling problem in a vessel of finite height. For this problem, the mixture-model equations have an exact solution which is used to validate the finite volume scheme for the dispersed phase. The second application treats spin-up from rest of a mixture of light particles in the absence of gravity. A previous numerical study of this problem is provided by Amberg and Ungarish (1993) and the results of the current method are easily compared to theirs. In addition, the flow close to the axis of rotation is essentially described by the classical von Kármán solution which is therefore used to validate the numerical discretisation of the non-linear advection terms. The third application is a study of gravity settling underneath a curved wall (the Boycott effect) for the intermediate parameter regime where both inertial and viscous effects are important. The study is used to demonstrate the generality of the numerical method to arbitrary configurations and the ability to use different resolution in different parts of the computational domain.

4.1. One-dimensional gravity settling

Consider a homogeneous mixture of heavy particles ($\varepsilon > 0$) separating vertically under the influence of gravity between two horizontal boundaries. As the particles move away from the upper boundary, a layer of clear fluid is produced in the upper part of the domain, and the particles settling on the lower boundary compact into a sediment. Let z^* denote the coordinate in the vertical direction and let the horizontal boundaries be located at $z^* = 0$ and $z^* = H^*$ respectively, where asterisks denote dimensional quantities. Assuming that the fluid is initially at rest, the continuity equation,

$$\frac{\mathrm{d}j_z^*}{\mathrm{d}z^*}, \tag{57}$$

together with the boundary conditions $j_z^* = 0$ at $z^* = 0, H^*$ gives,

$$j_z^* \equiv 0. \tag{58}$$

Hence, the balance in the momentum equation is purely hydrostatic. By scaling z^* with H^* and time with H^*/U_s^*, Eqs. (20)–(22) simplify into,

$$\frac{\partial \phi}{\partial t} + \frac{\partial \Phi(\phi)}{\partial z} = 0, \tag{59}$$

where

$$\Phi(\phi) = -\frac{\phi(1-\phi)^2}{\eta(\phi)}. \tag{60}$$

The solution to this problem is found by the method of characteristics as shown by Kynch (1952). Two kinematic shocks, separating regions of pure fluid and mixture, and mixture and sediment, form at the onset of the separation process. Hence, the volume fraction of particles in the mixture bulk remains at its initial value, which will be denoted by $\phi(0)$, and the shock-speed for the interface separating the pure-fluid region from the mixture bulk is given by,

$$\frac{\mathrm{d}z_\mathrm{p}}{\mathrm{d}t} = \frac{\Phi(\phi(0)) - \Phi(0)}{\phi(0) - 0} = \frac{\Phi(\phi(0))}{\phi(0)}, \tag{61}$$

where $z_\mathrm{p}(0) = 1$. The volume fraction on the lower boundary instantly reaches maximum packing (ϕ_M). Due to the particular choice of the expression for $\eta(\phi)$, a kinematic shock connecting the constant states $\phi(0)$ and ϕ_M does not satisfy the proper entropy condition. Instead, a weaker shock appears and the sediment region is described by a rarefaction wave in which the volume fraction smoothly approaches ϕ_M at the lower boundary. The flux function $\Phi(\phi)$ is shown in Fig. 3 together with a solid line connecting the states $\phi(0)$ and ϕ_M. The speed of the characteristics is given by the slope of Φ and the speed of the shock is given by the slope of the solid line. It is observed that for $\phi > 0.53$, the speed of the characteristics is less than the shock-speed and thus, the shock would move away from the characteristics. Also shown in Fig. 3 is the weaker shock

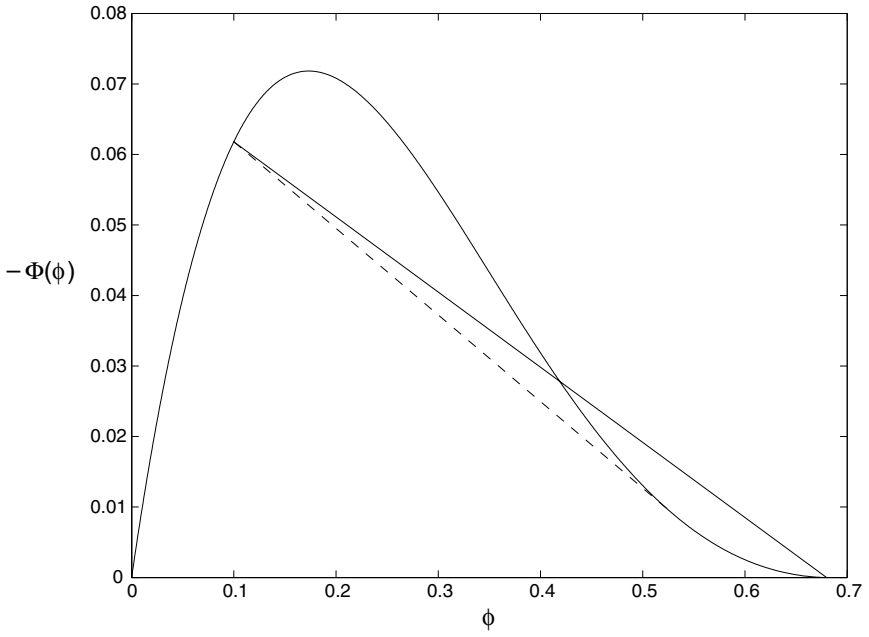

Fig. 3. The flux function $\Phi(\phi)$. Also shown is an entropy violating shock connecting the states $\phi(0)$ and ϕ_M (solid line) as well as a weaker shock satisfying the proper entropy condition (dashed line).

(the dashed line which is tangent to Φ at $\phi \approx 0.53$). The solution to the problem for $0 < t < t_{\text{final}}$, where t_{final} is the time when the mixture–pure fluid interface reaches the mixture–sediment interface, may be summarized as follows:

$$\phi(z,t) = 0 \quad \text{for } z_{\text{p}} < z < 1,$$
$$\phi(z,t) = \phi(0) \quad \text{for } z_{\text{s}} < z < z_{\text{p}},$$
$$\phi(z_{\text{s}},t) < \phi(z,t) < \phi_{\text{M}} \quad \text{for } 0 < z < z_{\text{s}},$$

where the position of the mixture–sediment interface is given by,

$$\frac{\mathrm{d}z_{\text{s}}}{\mathrm{d}t} = \frac{\Phi(\phi(z_{\text{s}},t)) - \Phi(\phi(0))}{\phi(z_{\text{s}},t) - \phi(0)} \tag{62}$$

with $z_{\text{s}}(0) = 0$. The volume fraction in the rarefaction wave is given by,

$$\phi(z,t) = \phi(z_{\text{c}}(t)) \quad \text{on } \frac{\mathrm{d}z_{\text{c}}}{\mathrm{d}t} = \frac{\mathrm{d}\Phi}{\mathrm{d}\phi}, \tag{63}$$

where

$$z_{\text{c}}(0) = 0 \quad \text{and} \quad \phi(z_{\text{s}},t) < \phi(z_{\text{c}}(t)) < \phi_{\text{M}}. \tag{64}$$

The value $\phi(z_{\text{s}},t)$, needed in Eq. (62), is obtained by applying a shooting method to find the characteristic $z_{\text{c}}(t) = z_{\text{s}}$ from Eqs. (63) and (64). The solution at $t = 1$ with $\phi(0) = 0.1$ and $\Phi(\phi)$ given by Eq. (60) is shown in Fig. 4 (solid line). Also shown is the result of the finite volume

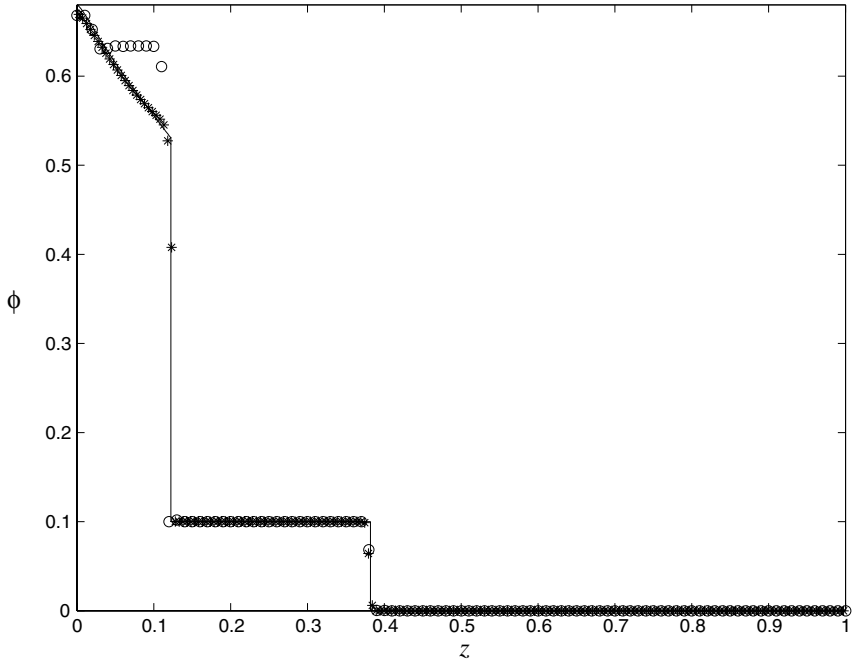

Fig. 4. The volume fraction field for one-dimensional gravity settling at $t = 1$. The solid curve represents the results of the characteristics method, the stars represent the results from the finite volume computation and the circles represent the results from the FEM-FCT computation.

scheme described in the previous section (stars). The computation was carried out on a regular grid with 100 grid points. In the finite volume computation, the volume fraction at the lower boundary is $\phi(0) = 0.1$ at $t = 0$. Since $\Phi \to 0$ as $\phi \to \phi_M$, it takes an infinite time to reach the value ϕ_M, and the values in the sediment region are therefore slightly lower than those predicted by the characteristics method. Both shock positions agree well with the characteristics method and the correct entropy condition is satisfied at the mixture–sediment interface. The shocks are smeared over a couple of grid points by the finite volume scheme. The circles in Fig. 4 represent the results of the original FEM-FCT scheme proposed by Löhner (1988), and it is immediately observed that this method is unable to satisfy the correct entropy condition at the mixture–sediment interface. The reason for this is that the FCT scheme is based on a centered collocation method where the only limitation on the second-order corrections is that no additional extrema are created. Hence, the point on the sediment side of the mixture–sediment interface is affected by the steepening effect of the shock which is really in the downwind direction, and this results in the plateau shown in Fig. 4. In the finite volume scheme, this phenomenon is avoided by choosing the upwind flux at each cell boundary. Although, the FEM-FCT scheme in this case is easily modified to give the correct entropy condition, such modifications become elaborate in higher dimensions and the finite volume scheme is therefore preferable for the current applications.

4.2. Spin-up from rest of a mixture

A cylindrical container filled with an initially uniform mixture of light particles (particles which have a lower density than the suspending fluid) is instantaneously set into rotation. Uniform non-rotating mixture is sucked in by the von Kármán layers on the horizontal boundaries where it gets spun-up and expelled radially outwards. The rotating mixture emerges from the boundary layers at the corners and thereby returns to the interior as spun-up fluid. At the same time the particles separate radially inward due to local centrifugal forces. The combination of these two effects gives the mixture–pure fluid interface a characteristic hour-glass-like shape (see Ungarish, 1991).

Consider a straight circular cylinder of height H^* and radius r_0^*, initially filled with a stationary mixture of light particles with constant volume fraction $\phi(0)$. Asterisks are again used to denote dimensional quantities. At time $t^* = 0$, the container is impulsively brought to a constant angular velocity Ω^* around its axis of symmetry. Effects of gravity are neglected in the analysis. The equations of motion are made non-dimensional by the following scales: r_0^* for length, $1/\Omega^*$ for time, $\Omega^* r_0^*$ for flux densities, ρ_C^* for density and $\rho_C^*(\Omega^* r_0^*)^2$ for pressure:

$$\frac{\partial \mathbf{j}}{\partial t} + \mathbf{j}\cdot\nabla\mathbf{j} = -\nabla p + E\nabla\cdot[\eta(\phi)(\nabla\mathbf{j} + (\nabla\mathbf{j})^{\mathrm{T}})] - \nabla\cdot\left[\frac{\mathbf{j}_R\mathbf{j}_R}{\phi(1-\phi)}\right] - \varepsilon\left[\frac{\partial \mathbf{j}_d}{\partial t} + \nabla\cdot\left(\frac{\mathbf{j}_d\mathbf{j}_d}{\phi}\right)\right], \tag{65}$$

$$\nabla\cdot\mathbf{j} = 0, \tag{66}$$

$$\frac{\partial\phi}{\partial t} + \nabla\cdot\mathbf{j}_d = 0, \tag{67}$$

$$\mathbf{j}_R = -\frac{\varepsilon\beta\phi(1-\phi)^2}{\eta(\phi)}\left[\frac{\partial\mathbf{j}}{\partial t} + \mathbf{j}\cdot\nabla\mathbf{j}\right], \tag{68}$$

$$\mathbf{j}_d = \mathbf{j}_R + \phi\mathbf{j}, \tag{69}$$

where the non-dimensional numbers

$$E = \frac{v_0^*}{\Omega^* r_0^{*2}}, \quad \varepsilon = \frac{\rho_d^* - \rho_C^*}{\rho_C^*} \quad \text{and} \quad \beta = \frac{2\Omega^* a^{*2}}{9 v_0^*} \tag{70}$$

are the Ekman number, the relative density difference and the particle Taylor number respectively. In the limit of $E \ll 1$ and $|\varepsilon|\phi(0) \ll 1$, Ungarish (1991) derived the following expressions for the volume fraction in the two regions separated by the spin-up front ($r = e^{-\tau}$):

$$\frac{\partial\phi}{\partial\tau} - r\frac{\partial\phi}{\partial r} + (2z - H)\frac{\partial\phi}{\partial z} = 0, \quad 0 \leqslant r \leqslant e^{-\tau}, \tag{71}$$

$$\frac{\partial\phi}{\partial\tau} + \frac{1}{r(1 - e^{-2\tau})}\left((r^2 - 1)e^{-2\tau} - \frac{1}{\lambda\mathscr{M}}\frac{(r^2 - e^{-2\tau})^2}{r^2(1 - e^{-2\tau})}\frac{d}{d\phi}\left[\frac{\phi(1-\phi)^2}{\eta(\phi)}\right]\right)\frac{\partial\phi}{\partial r}$$
$$- \frac{(2z - H)e^{-2\tau}}{1 - e^{-2\tau}}\frac{\partial\phi}{\partial z} = \frac{2}{\lambda\mathscr{M}}\frac{\phi(1-\phi)^2}{\eta(\phi)}\frac{(1 - e^{-4\tau}/r^4)}{(1 - e^{-2\tau})^2} \quad e^{-\tau} \leqslant r \leqslant 1, \tag{72}$$

where

$$\mathscr{M} = (\eta[\phi(0)])^{1/2}, \quad \tau = \frac{\mathscr{M}E^{1/2}t}{H} \quad \text{and} \quad \lambda = \frac{E^{1/2}}{|\varepsilon|\beta H}. \tag{73}$$

In the first region (the non-rotating core) the solution is $\phi = \phi(0)$. The corresponding expressions for the velocity field in this region describe a flow from the interior towards the top and bottom boundaries. At the plates, the fluid is absorbed by the boundary layers where it gets spun-up and expelled radially outwards. When the spun-up fluid reaches the corners of the container, $r = 1$, $z = 0, H$, it emerges from the boundary layers into the second region (the region behind the spin-up front). Hence, the fluid which enters into this region has an initial particle volume fraction of $\phi(0)$. The solution for the dispersed phase in the second region is readily found by the method of characteristics resulting in a set of ordinary differential equations, which were solved numerically using a shooting method.

The following parameters were used in the full numerical simulation: aspect ratio $H = H^*/r_0^* = 0.5$, Ekman number $E = 10^{-4}$, particle Taylor number $\beta = 4 \times 10^{-2}$, reduced density difference $\varepsilon = -0.5$ and initial volume fraction $\phi(0) = 0.1$. These parameters which were picked from Amberg and Ungarish (1993) make the ratio of the separation to spin-up time-scales, $\lambda = E^{1/2}/(|\varepsilon|\beta H)$, equal to 1. The simulation was carried out up to $t = 150$ (corresponding to about 24 revolutions of the container) on a regularly triangulated grid with 128 radial boundary points and 64 axial boundary points. The time-step was chosen to be $\Delta t = 2.5 \times 10^{-2}$. The results of the asymptotic theory (the numerical solution of Eqs. (71) and (72)) have been reproduced here and are presented together with the numerical results. Fig. 5 shows contours of constant volume fraction at $t = 25$, 50, 75, 100. Only the region $0 \leqslant z \leqslant H/2$ is displayed because of symmetry. In the non-rotating core there is no centrifugal force and therefore no separation takes place in this region. According to the theory, the extent of the non-rotating core diminishes asymptotically with time and the spin-up front remains sharp. More advanced analyses on spin-up of a pure fluid (Venezian, 1970; Hyun et al., 1983) show that the front is actually smeared by viscous effects. This

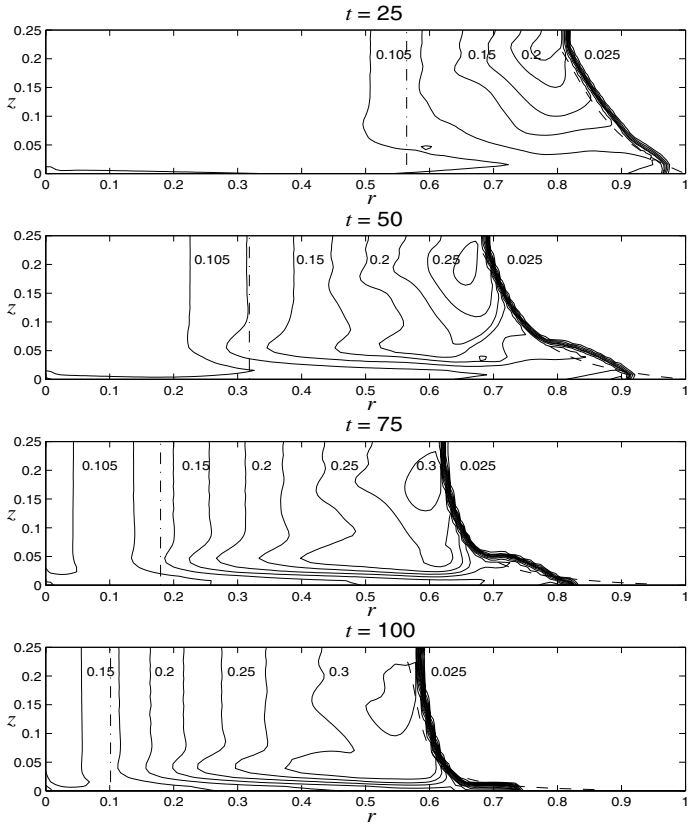

Fig. 5. Contours of constant ϕ for various t. The levels are 0.025, 0.050, 0.075, 0.095, 0.105, 0.125, ... (0.025). Also shown are the asymptotic spin-up front (dash-dotted) and kinematic shock (dashed).

is also observed in the numerical results. At $t = 50$, the region where the volume fraction varies with spatial position extends significantly beyond the theoretically predicted spin-up front. Already at $t = 100$, the fluid is in solid-body rotation and the interface separating the mixture from the pure fluid has become almost cylindrical. The subsequent motion is of a different nature and the results of the asymptotic analysis are no longer relevant. At $t = 150$ (the end of the simulation), the final state of a solid particle core has not yet been reached. Hence, there is still a positive radial gradient in the volume fraction.

In the asymptotic analysis, presented by Ungarish (1991), it was assumed that the volume fraction of particles in the boundary layers at the top and bottom plates remained uniform and equal to the initial value ($\phi = \phi(0)$). Since the radial outflow in the boundary layers decays with both r and t, there is a radial position where the inward particle flux due to the local centrifugal force becomes stronger than the outward boundary layer flux. Note that this critical value also varies with vertical distance from the horizontal boundaries according to the local boundary layer profiles. For radii larger than the critical value, centrifugal settling occurs, resulting in an increase in volume fraction. The volume fraction in the part of the boundary layers above and beneath the non-rotating interior only differs slightly from $\phi(0)$, with deviations being less

than 5%. At $t = 25$, the volume fraction in the parts of the boundary layers adjacent to the rotating part of the mixture increases with about 20%. At $t = 50$, the deviations are 50% and at $t = 75$, they are 100%, which corresponds to a 38% increase in the effective viscosity. At this time, spin-up is essentially complete. Despite the substantial violations of the uniform volume fraction assumption, the position of the analytically predicted kinematic shock is in good agreement with the numerical results throughout the spin-up process. A quantitative comparison between the numerically and analytically predicted radial distributions of the volume fraction at time $t = 50$ and axial position $z = 0.225$ is given in Fig. 6. The theoretical shock is sharp while the numerical shock is smeared over two or three grid points due to artificial diffusion inherent in the discretisation scheme. The results obtained here are in excellent agreement with those presented in Amberg and Ungarish (1993), where experimental results also were provided for qualitative comparison with asymptotic theory and numerical simulations. Figs. 5 and 6 correspond to Figs. 6 and 10(a) in Amberg and Ungarish (1993). Fig. 5 displays two notable differences between the current results and those in Amberg and Ungarish (1993), both of which may be attributed to the higher-order finite volume scheme for the dispersed phase. The first one is that the region with the highest volume fraction is observed to move away from the centerline as the mixture approaches solid-body rotation. At this stage, the boundary layer efflux diminishes and the radial mixture motion in the interior becomes restricted by geostrophic effects. Hence, recirculation of dispersed matter through mixture motion becomes gradually confined to thin regions adjacent to the horizontal boundaries and the separation front. These layers are now of the Ekman type and the characteristic oscillatory behavior is observed for the horizontal layers. The second difference is the appearance of isolated regions with slightly lower concentrations at $r \approx 0.6$ for $t = 25$ and at $r \approx 0.68$ for $t = 50$. In both cases these regions are trapped within the vortex separating the influx part of the horizontal boundary layers from the efflux part. A close-up of the concentration contours together with velocity vectors for the mixture fluid at $t = 50$ is shown in Fig. 7.

At early times, the horizontal boundary layers above and beneath the non-rotating core are essentially of the von Kármán type. This provides a convenient means for validating the numerical treatment of the non-linear terms. Since the boundary layers are being fed from the interior, the only modifications to the classical solution comprise of uniform enhancements of the density and viscosity (due to the presence of particles), and an adjustment of the boundary

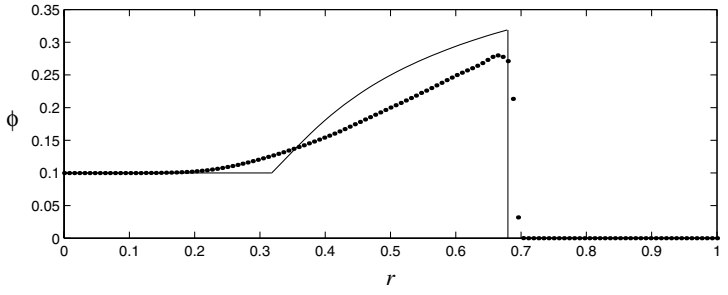

Fig. 6. Radial volume fraction distribution at time $t = 50$ and $z = 0.225$. The solid line represents the result of the asymptotic theory while the dots represent the result of the numerical simulation.

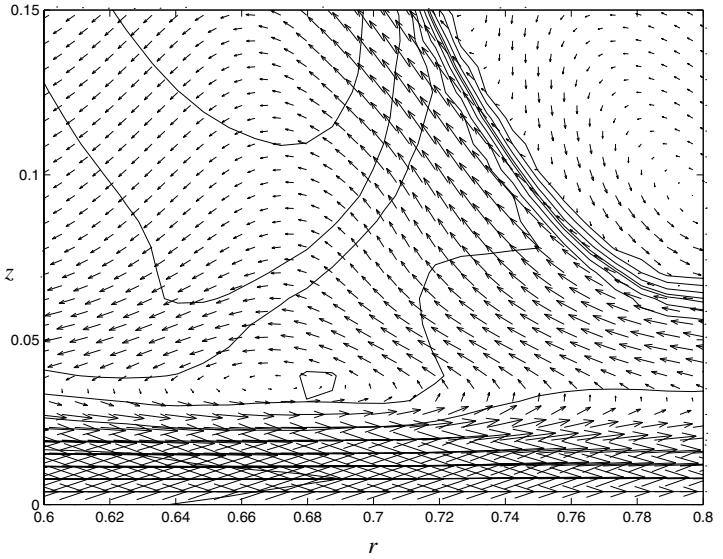

Fig. 7. Close-up of an isolated region with slightly lower concentration at $t = 50$. The solid lines represent concentration contours (see Fig. 5 for labeling) and the arrows represent velocity vectors for the mixture fluid.

condition to comply with the restriction of no net flux across a radial cross-section of the vessel. Introducing the following radial dependence for the quasi-steady velocity components and pressure:

$$u(r,z) = rF\left(\frac{z}{\sqrt{\mathscr{E}}}\right), \quad v(r,z) = rG\left(\frac{z}{\sqrt{\mathscr{E}}}\right), \quad w(r,z) = \sqrt{\mathscr{E}}H\left(\frac{z}{\sqrt{\mathscr{E}}}\right),$$
$$p(r,z) = K\frac{r^2}{2} + \mathscr{E}L\left(\frac{z}{\sqrt{\mathscr{E}}}\right), \tag{74}$$

where $\mathscr{E} = \eta(\phi(0))E/(1+\varepsilon\phi(0))$, Eqs. (65) and (66) reduce to,

$$F'' = F^2 + HF' - G^2 + K, \tag{75}$$
$$G'' = 2FG + HG', \tag{76}$$
$$H'' = HH' + L', \tag{77}$$
$$H' = -2F, \tag{78}$$

upon neglecting terms of $O(\beta)$. The boundary conditions are given by,

$$F(0) = 0, \quad G(0) = 1, \quad H(0) = 0, \quad G\left(\frac{1}{4\sqrt{\mathscr{E}}}\right) = 0, \quad H\left(\frac{1}{4\sqrt{\mathscr{E}}}\right) = 0, \tag{79}$$

recalling that the center of the vessel is at $z = 0.25$. By virtue of Eq. (78) and the third condition in (79), the last boundary condition is equivalent to the requirement $\int_{z=0}^{z=0.25} F\,\mathrm{d}z = 0$ (no net flux

through a radial cross-section). Eq. (78) was used to eliminate F from Eqs. (75) and (76), which were subsequently solved by a fourth-order accurate Runge–Kutta scheme, applying a shooting method to satisfy the boundary conditions at $z = 0.25$. A comparison between the von Kármán solution and the numerical solution at $t = 25$ and $r = 0.25$ is shown in Fig. 8. Despite the relatively small number of discretisation points in the boundary layer, the agreement is excellent. Ungarish and Greenspan (1983) (see also Ungarish, 1993, Section 5.4) studied the semi-infinite Kármán problem in the context of the two-fluid model. Applying a perturbation expansion in the Taylor number β, they encountered difficulties when applying the no-flux condition at $O(\beta)$, which were attributed to a mathematical deficiency in the formulation. The current mixture-model analysis corresponds to the well-posed leading order problem ($O(1)$), which becomes identical to the two-fluid formulation if the viscosities of both phases are taken to be equal. The numerical simulations did not display any problematic behavior at the top and bottom boundaries. This might indicate that the mixture model does not suffer from a similar deficiency.

Further validation for the non-linear terms was obtained by showing consistency (to the order of the numerical discretisation error) between numerical simulations performed in the rotating and non-rotating reference frames.

4.3. The Boycott effect

Due to its importance in achieving enhanced settling performance in separation processes, the Boycott effect has become the subject of numerous studies including Acrivos and Herbolzheimer

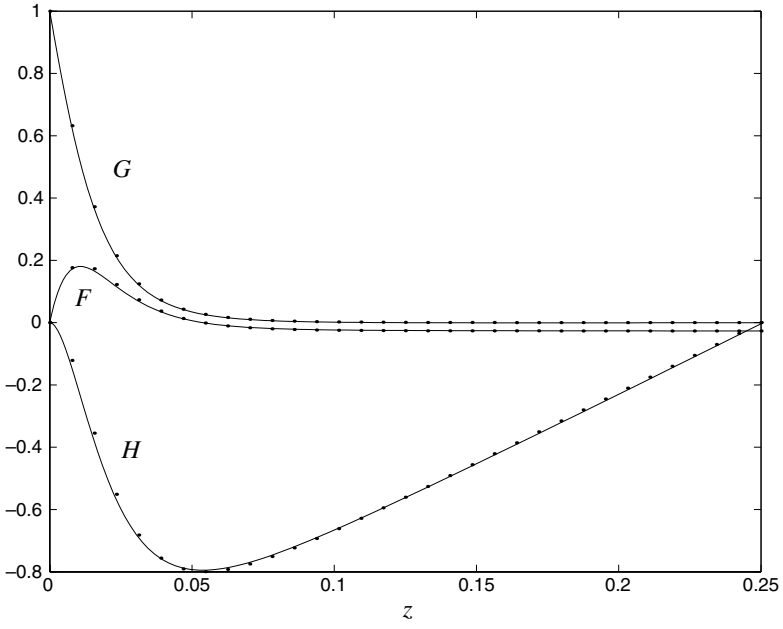

Fig. 8. Kármán-layer profiles at $t = 25$ and $r = 0.25$. The solid lines represent the results from asymptotic theory and the dots represent the results from the numerical simulation.

(1979), Hill et al. (1977), Schneider (1982) and Shaqfeh and Acrivos (1986). When a mixture of heavy particles settles under gravity away from an inclined wall, a thin layer of pure fluid develops next to the wall. This layer remains thin for the duration of the sedimentation process due to a balance between buoyancy forces and inertial and/or viscous forces. The buoyant particle-free fluid in the thin layer rises along the inclined wall at a velocity which is considerably higher than that of the settling particles in the mixture. Volume conservation requires that this fluid must be replaced by pure fluid from the mixture bulk. The flow into the pure fluid region counteracts the gravitational settling of the particles and thus prevents the layer from growing. The persistence of a thin pure-fluid layer leads to an increase in the area of the mixture–pure fluid interface. Because the rate of separation is proportional to the horizontal projection of the mixture–pure fluid interface, this effect reduces the total separation time. Much of the literature has been concerned with the details of the Boycott layer, but the flow in the mixture bulk and especially the flow reversal in the pure-fluid region developing at the top of the container have received little attention. An interesting variant of the Boycott effect has been observed (Schaflinger, 1997) in a container with a curved wall. The numerical simulation presented in this section resolves the details of the Boycott layer underneath a curved wall as well as the complex dynamics of the horizontal mixture–pure fluid interface.

Consider an initially uniform mixture of volume fraction $\phi(0)$, separating under gravity in a vessel of height H^*, width L^* and a curved wall with radius $R^* = H^*$ (see Fig. 9). Here, z_f^* denotes the vertical location of the horizontal separation front (the horizontal section of the mixture–pure fluid interface). A non-dimensional form of the equations appropriate for numerical simulations is obtained by introducing the following scaling: H^* for length, $U^* = (|\varepsilon|\phi(0)g^*H^*)^{1/2}$ for velocity, H^*/U^* for time, ρ_C^* for density and $|\varepsilon|\phi(0)\rho_C^* g^* H^*$ for pressure:

$$\frac{\partial \mathbf{j}}{\partial t} + \mathbf{j}\cdot\nabla\mathbf{j} = -\nabla p - \frac{\phi}{\phi(0)}\hat{\boldsymbol{z}} + \frac{1}{\sqrt{Re\,\Lambda}}\nabla\cdot[\eta(\phi)(\nabla\mathbf{j} + (\nabla\mathbf{j})^{\mathrm{T}})] - \nabla\cdot\left[\frac{\mathbf{j}_R\mathbf{j}_R}{\phi(1-\phi)}\right] - \varepsilon\left[\frac{\partial \mathbf{j}_d}{\partial t} + \nabla\cdot\left(\frac{\mathbf{j}_d\mathbf{j}_d}{\phi}\right)\right], \tag{80}$$

$$\nabla\cdot\mathbf{j} = 0, \tag{81}$$

$$\frac{\partial\phi}{\partial t} + \nabla\cdot\mathbf{j}_d = 0, \tag{82}$$

$$\mathbf{j}_R = -\sqrt{\frac{Re}{\Lambda}}\frac{\phi(1-\phi)^2}{\eta(\phi)}\left[|\varepsilon|\phi(0)\left(\frac{\partial\mathbf{j}}{\partial t} + \mathbf{j}\cdot\nabla\mathbf{j}\right) + \hat{\boldsymbol{z}}\right], \tag{83}$$

$$\mathbf{j}_d = \mathbf{j}_R + \phi\mathbf{j}. \tag{84}$$

The non-dimensional parameters are given by

$$Re = \frac{U_s^* H^*}{v_0^*} = \frac{2|\varepsilon|a^{*2}g^*H^*}{9v_0^{*2}} \quad \text{and} \quad \Lambda = \frac{9}{2}\left(\frac{H^*}{a^*}\right)^2\phi(0), \tag{85}$$

where the Reynolds number is based on the settling velocity, U_s^*, of a single particle. The enhancement in the settling rate is obtained from PNK theory (Ponder, 1925; Nakamura and Kuroda, 1937) as the ratio of the horizontal projection of the mixture–pure fluid interface to the

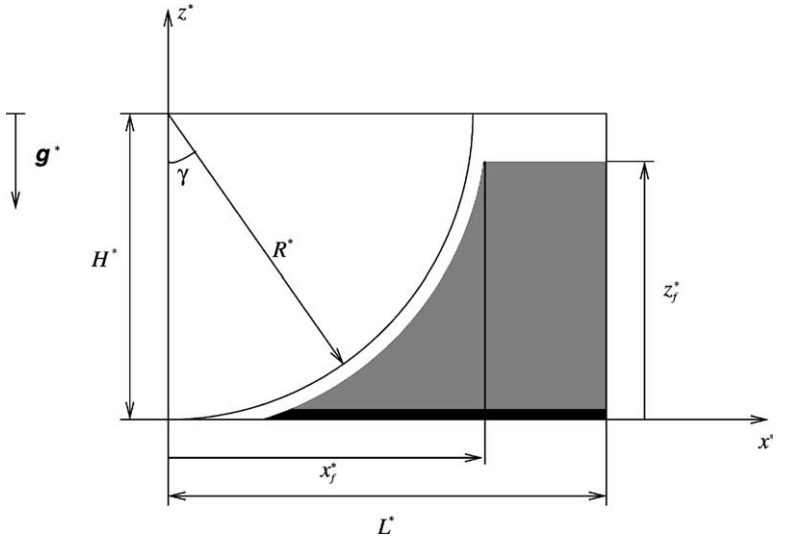

Fig. 9. Geometric set-up for the inclined settling problem.

horizontal section of the mixture–pure fluid interface. Neglecting the width of the Boycott layer, this yields

$$\frac{\mathrm{d}z_\mathrm{f}}{\mathrm{d}t} = -\sqrt{\frac{Re}{\Lambda}}\mathscr{A}\frac{L}{L-x_\mathrm{f}}, \tag{86}$$

where $\mathscr{A} = (1-\phi(0))^2/\eta(\phi(0))$. Eq. (86) may be integrated to obtain an implicit expression for z_f,

$$z_{\mathrm{f}0} - z_\mathrm{f} - \frac{1}{2L}\sin^{-1}(z_{\mathrm{f}0}-z_\mathrm{f}) - \frac{z_{\mathrm{f}0}-z_\mathrm{f}}{2L}\sqrt{1-(z_{\mathrm{f}0}-z_\mathrm{f})^2} = \sqrt{\frac{Re}{\Lambda}}\mathscr{A}(t-t_0), \tag{87}$$

where $z_{\mathrm{f}0}$ is the position of the interface at time $t = t_0$. Thus, in terms of the current scaling, the separation time is $\mathrm{O}((\Lambda/Re)^{1/2})$, and the inverse of the separation time is the appropriate small parameter to be used in a thin-layer approximation. Such approximations lead to quasi-steady pure-fluid layers within which similarity solutions for the dependent flow variables can be derived. Three qualitatively different parameter regimes with different scalings for the width δ of the Boycott layer have been identified:

(a) The buoyancy driving is counteracted by viscous forces, while inertia is negligible

$$Re \ll \Lambda^{1/3}, \quad \delta \sim \Lambda^{-1/3}.$$

(b) The buoyancy driving is counteracted by inertial forces, while viscosity is negligible

$$\Lambda^{1/3} \ll Re \ll \Lambda, \quad \delta \sim (Re/\Lambda)^{1/2}.$$

(c) All three terms are of comparable orders of magnitude

$$Re \sim \Lambda^{1/3}, \quad \delta \sim \Lambda^{-1/3} \sim (Re/\Lambda)^{1/2}.$$

For vessels with constant inclination, Acrivos and Herbolzheimer (1979) developed a theory for case (a) while Schneider (1982) analyzed case (b). The gap (case (c)) was later bridged by Shaqfeh and Acrivos (1986), who derived asymptotic expansions for all parameter regimes under the assumption that $(Re/\Lambda)^{1/2} \ll 1$. To present date, no attempt has been made to extend the analysis of Shaqfeh and Acrivos (1986) to vessels with curved boundaries. The remainder of this section is devoted to the intermediate Reynolds number case ($Re \sim \Lambda^{1/3}$). In the limit when $\delta/R \ll 1$, the leading order boundary value problem in the Boycott layer reduces to (see Ungarish, 1993, Section 6.3),

$$\frac{\partial\psi}{\partial\zeta}\frac{\partial^2\psi}{\partial\xi\,\partial\zeta} - \frac{\partial\psi}{\partial\xi}\frac{\partial^2\psi}{\partial\zeta^2} = \sin\gamma(\xi) + \Lambda^{-2/3}\frac{\partial^3\psi}{\partial\zeta^3}, \tag{88}$$

$$\psi = \frac{\partial\psi}{\partial\zeta} = 0 \quad \text{at } \zeta = 0, \tag{89}$$

$$\psi = \Lambda^{-1/3}\mathscr{A}\int_0^{\xi}\cos\gamma(\xi')\,\mathrm{d}\xi' \quad \text{at } \zeta = \delta(\xi), \tag{90}$$

where the Reynolds number was chosen to be $Re = \Lambda^{1/3}$, and ξ and ζ are the coordinates along and orthogonal to the curved wall respectively. In the numerical simulation, the radius was taken to be $R = 1$ for which $\gamma(\xi) = \xi$. The flow field in the mixture region adjacent to the Boycott layer is similarly described by,

$$(1+\varepsilon\phi(0))\left(\frac{\partial\bar{\psi}}{\partial\zeta}\frac{\partial^2\bar{\psi}}{\partial\xi\,\partial\zeta} - \frac{\partial\bar{\psi}}{\partial\xi}\frac{\partial^2\bar{\psi}}{\partial\zeta^2}\right) = \Lambda^{-2/3}\eta(\phi(0))\frac{\partial^3\bar{\psi}}{\partial\zeta^3}, \tag{91}$$

$$\bar{\psi} = \psi, \quad \frac{\partial\bar{\psi}}{\partial\zeta} = \frac{\partial\psi}{\partial\zeta} \quad \text{and} \quad \eta(\phi(0))\frac{\partial^2\bar{\psi}}{\partial\zeta^2} = \frac{\partial^2\psi}{\partial\zeta^2} \qquad \text{at } \zeta = \delta(\xi), \tag{92}$$

$$\frac{\partial\bar{\psi}}{\partial\zeta} \to 0 \quad \text{as } \zeta \to \infty. \tag{93}$$

Note that Eqs. (89), (90), (92) and (93) provide seven boundary/matching conditions at $\zeta = 0$, $\delta(\xi)$ and ∞ whereas the equations for ψ and $\bar{\psi}$ are both third order in ζ. The additional condition determines the width $\delta(\xi)$ of the Boycott layer. Solutions to the two boundary value problems are expanded in Blasius series,

$$\psi(\xi,\zeta) = \Lambda^{-1/3}\mathscr{A}\left(\xi f_1\left(\frac{\zeta}{\delta(\xi)}\right) - \frac{\xi^3}{3!}f_3\left(\frac{\zeta}{\delta(\xi)}\right) + \frac{\xi^5}{5!}f_5\left(\frac{\zeta}{\delta(\xi)}\right) - \cdots\right), \tag{94}$$

$$\bar{\psi}(\xi,\zeta) = \Lambda^{-1/3}\mathscr{A}\left(\xi \bar{f}_1\left(\frac{\zeta}{\delta(\xi)}\right) - \frac{\xi^3}{3!}\bar{f}_3\left(\frac{\zeta}{\delta(\xi)}\right) + \frac{\xi^5}{5!}\bar{f}_5\left(\frac{\zeta}{\delta(\xi)}\right) - \cdots\right), \tag{95}$$

$$\delta(\xi) = \Lambda^{-1/3}\delta_0\left(1 - \frac{\xi^2}{2!}\delta_2 + \frac{\xi^4}{4!}\delta_4 - \cdots\right). \tag{96}$$

The equations for the first three terms are obtained as,

$$f_1''' = \mathscr{A}\delta_0[f_1'^2 - f_1 f_1''] - \frac{\delta_0^3}{\mathscr{A}}, \tag{97}$$

$$\bar{f}_1''' = \mathscr{B}\delta_0[\bar{f}_1'^2 - \bar{f}_1\bar{f}_1''], \tag{98}$$

$$f_3''' = \mathscr{A}\delta_0[4f_1'f_3' - f_1 f_3'' - 3f_1''f_3 - 3\delta_2(f_1'^2 + f_1 f_1'')] - \frac{\delta_0^3}{\mathscr{A}}(1 + 9\delta_2), \tag{99}$$

$$\bar{f}_3''' = \mathscr{B}\delta_0[4\bar{f}_1'\bar{f}_3' - \bar{f}_1\bar{f}_3'' - 3\bar{f}_1''\bar{f}_3 - 3\delta_2(\bar{f}_1'^2 + \bar{f}_1\bar{f}_1'')], \tag{100}$$

$$\begin{aligned} f_5''' = {} & \mathscr{A}\delta_0[6f_1'f_5' + 10f_3'^2 - f_1 f_5'' - 5f_1''f_5 - 10f_3 f_3'' - 10\delta_2(f_1 f_3'' + 3f_1''f_3) \\ & - 5\delta_4(3f_1'^2 + f_1 f_1'')] - \frac{\delta_0^3}{\mathscr{A}}(1 + 30\delta_2 + 15\delta_4 + 90\delta_2^2), \end{aligned} \tag{101}$$

$$\begin{aligned} \bar{f}_5''' = {} & \mathscr{B}\delta_0[6\bar{f}_1'\bar{f}_5' + 10\bar{f}_3'^2 - \bar{f}_1\bar{f}_5'' - 5\bar{f}_1''\bar{f}_5 - 10\bar{f}_3\bar{f}_3'' - 10\delta_2(\bar{f}_1\bar{f}_3'' + 3\bar{f}_1''\bar{f}_3) \\ & - 5\delta_4(3\bar{f}_1'^2 + \bar{f}_1\bar{f}_1'')], \end{aligned} \tag{102}$$

where $\mathscr{B} = (1 + \varepsilon\phi(0))(1 - \phi(0))^2/\eta^2(\phi(0))$, and the boundary/matching conditions are given by,

$$\begin{aligned} & f_i(0) = f_i'(0) = 0, \quad f_i(1) = \bar{f}_i(1) = 1, \quad f_i'(1) = \bar{f}_i'(1), \\ & f_i''(1) = \eta(\phi(0))\bar{f}_i''(1), \quad \bar{f}_i'(\infty) = 0. \end{aligned} \tag{103}$$

The boundary value problems were solved using a shooting method. In the numerical simulation presented below, the reduced density difference and the initial concentration were taken to be $\varepsilon = 0.1$ and $\phi(0) = 0.1$ which gives the following values:

$$f_1''(0) = 4.26760, \quad \delta_0 = 1.65419, \tag{104}$$

$$f_3''(0) = 6.10840, \quad \delta_2 = 0.109253, \tag{105}$$

$$f_5''(0) = 22.4316, \quad \delta_4 = 0.263938, \tag{106}$$

to within a tenth of a percent. The series converge rapidly and the difference between using two or three terms was hardly distinguishable within the range of ξ values for which comparisons with the numerical results were made.

In the numerical simulation, a higher concentration of nodes was used in the vicinity of the curved wall. Adequate resolution of the mixture–pure fluid interface and velocity profiles in the Boycott layer was obtained using 23 869 grid points. Dependent variables were saved at times $\tau = t(Re/\Lambda)^{1/2} = 1/96, 1/48, \ldots (1/96) \ldots, 1$. The computations were carried out for a container with aspect ratio (width to height) $L = 1.4$ and radius $R = 1$. The parameters were chosen to be: $\Lambda = 10^5$, $\varepsilon = 10^{-2}$, $\phi(0) = 0.1$ and Reynolds number $Re = \Lambda^{1/3}$. The time-step for the Stokes solver was chosen to be $\Delta t = 10^{-2}$, and the time-step for the advection and volume fraction problems was chosen to be six times smaller in order to comply with the CFL condition.

Fig. 10 shows the initial breakthrough of the Boycott layer into the region of pure fluid at the top of the vessel. The strong efflux from the Boycott layer pushes a thin layer of particles from the horizontal mixture–pure fluid interface up into the region of pure fluid and subse-

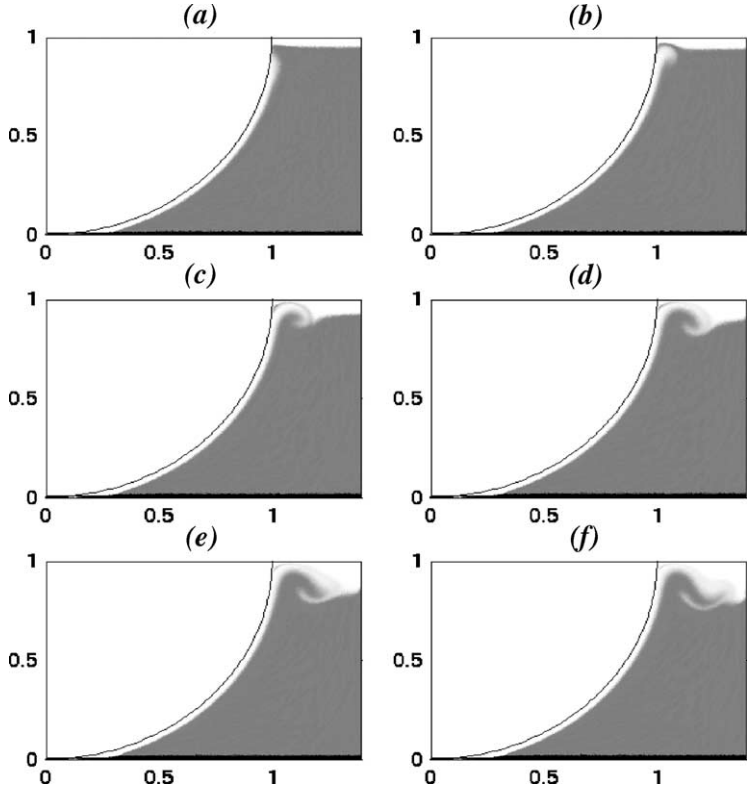

Fig. 10. Volume fraction (gray-scale) of particles during the initial breakthrough of the Boycott layer into the pure fluid region at the top of the vessel, $\tau = 1/12,\ 3/32, \ldots (1/96) \ldots$

quently keeps the particles suspended (Fig. 10(a)–(c)) for a short time-interval. As the efflux is reversed into the mixture region by a vortex localized to the top of the Boycott layer, it breaks through the mixture–pure fluid interface and entrains into the mixture bulk (Fig. 10(d)–(f)). Shortly after having been formed, the particle depleted region inside the mixture bulk starts to shrink, and eventually disappears. The reason for this is that the particles at the top of this region settle in pure fluid and therefore faster than the ones at the bottom of the region where hindrance effects due to the other particles in the mixture bulk come into play.

Fig. 11 shows concentration contours and streamlines at times $\tau = 1/8$, 3/8 and 5/8. At an early stage the flow in the mixture bulk bears a strong resemblance to that predicted by Schneider (1982) for the high Reynolds number case. Schneider showed that the vertical velocity in the mixture bulk is independent of the horizontal coordinate to leading order. Using the continuity equation and applying the normal flux conditions at the Boycott interface, the vertical wall and the mixture–sediment interface, he obtained a purely kinematic solution qualitatively similar to the one shown in Fig. 11(b). At later times, a characteristic feature of the flow field is the localized vortex at the top of the Boycott layer causing a strong deformation of the horizontal mixture–pure fluid interface, and a second vortex (Fig. 11(d)) which is oscillating back and forth between the vertical wall and the reversing primary vortex. As an

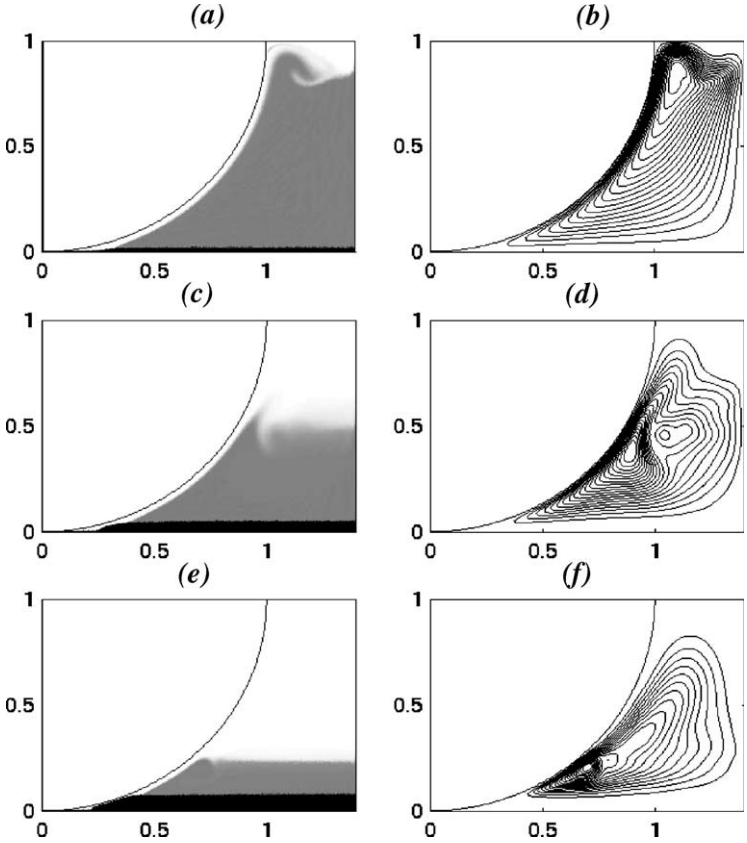

Fig. 11. Volume fraction (gray-scale) and streamlines for the mixture velocity at (a)–(b) $\tau = 1/8$, (c)–(d) $\tau = 3/8$, (e)–(f) $\tau = 5/8$.

effect of the interaction between the two vortices and the hindered settling process, the interface becomes stratified (Fig. 11(c)). Since the flux in the Boycott layer increases with its length (Eq. (90)), the strength of the vortices and the corresponding deformation of the interface decreases with time. At this stage the interface starts to gradually become sharper due to hindered settling effects (Fig. 11(e)). The volume fraction in the sediment region at the bottom of the container is described by a rarefaction wave of the same type as in the one-dimensional settling problem. Figs. 10 and 11 imply that the Boycott layer along the curved wall has constant thickness. This is in agreement with the leading order result of the Blasius series expansion (Eq. (96)). In the viscous limit ($Re \ll \Lambda^{1/3}$), the Boycott layer in the present configuration has a constant thickness $\delta_{\text{visc}} = 3^{1/3} \approx 1.44225$ (see Ungarish, 1993, Section 6.3 or Holmqvist, 1998) which is less than 13% smaller than that obtained here ($\delta_0 \approx 1.65419$). Fig. 12 shows the position of the mixture–pure fluid interface together with the results from PNK theory (Eq. (87)). The theoretical position (the solid line) has been adjusted for the initial transient (the formation of the Boycott layer). The point (t_0, z_{f0}) in Eq. (87) was taken directly from the numerical simulation. The reason why the numerical interface lags behind becomes evident by

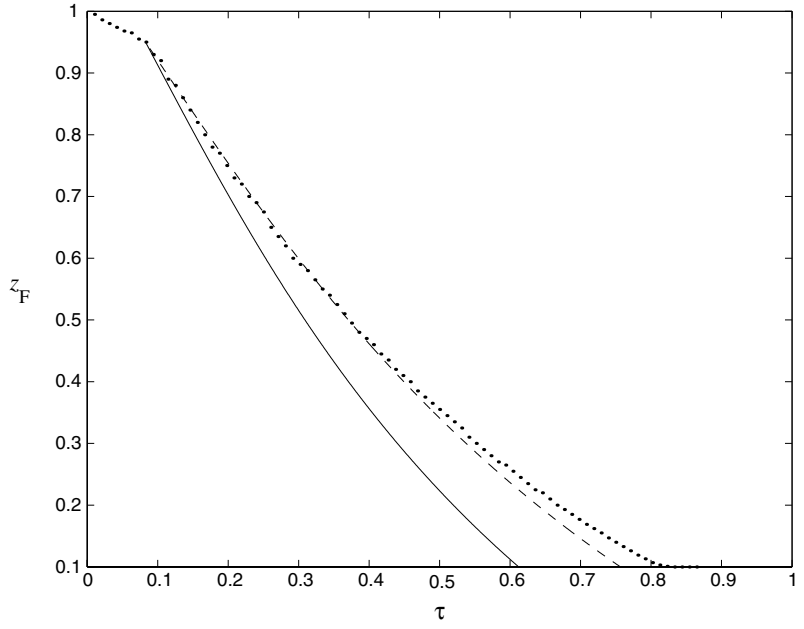

Fig. 12. Position of the mixture–pure fluid interface. The solid line represents the results from PNK theory, the dashed line PNK theory adjusted for the finite width of the Boycott layer and the dots represent the numerical results.

taking a closer look at Fig. 10 or 11. The finite width of the Boycott layer reduces the horizontal projection of the mixture–pure fluid interface and Eq. (86) must accordingly be modified to,

$$\frac{\mathrm{d}z_\mathrm{f}}{\mathrm{d}t} = -\sqrt{\frac{Re}{\Lambda}}\mathscr{A}\frac{L-x_0}{L-x_\mathrm{f}} = -\Lambda^{-1/3}\mathscr{A}\frac{L-x_0}{L-x_\mathrm{f}}, \tag{107}$$

where $Re = \Lambda^{-1/3}$ was substituted in and x_0 is the intersection of the Boycott interface with the mixture–sediment interface. Taking $x_0 \approx (2\Lambda^{-1/3}\delta_0)^{1/2} \approx 0.3$ (from Eq. (104)) gives the dashed line in Fig. 12. Comparisons of the streamwise velocity profile in the Boycott layer and the adjacent mixture region obtained from the numerical simulation and the Blasius series expansions (starting at $\xi = x_0$) are shown in Fig. 13. The adjustment to similarity behavior is observed to be slow. Although the Boycott layer rapidly adjusts to its near constant width, the viscous sublayer next to the curved wall grows more slowly and may even have a fractional power dependence on ξ as in the case of constant inclination (Shaqfeh and Acrivos, 1986). In addition, for small angles, the flow in the Boycott layer is strongly influenced by the flow in the mixture bulk and condition (93) is not applicable.

The Boycott effect is a fundamental phenomenon in separation theory. It is therefore essential that the basic flow scales are accurately reproduced in the numerical simulations. It should be noted that no additional constraints were necessary to obtain the quasi-steady pure-fluid layer in the simulation presented in this section. The Boycott simulation was repeated on the same grid

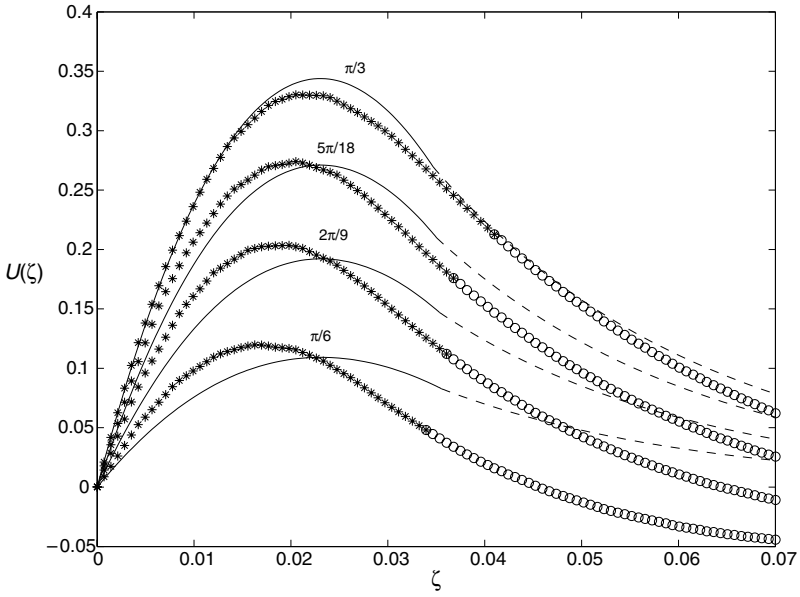

Fig. 13. Tangential velocity at $\tau = 1/6$ for a few positions along the curved wall. The solid and dashed curves represent the similarity expansions in the Boycott layer and adjacent mixture region respectively, and the stars and circles represent the corresponding numerical profiles.

with the FEM-FCT scheme (Löhner, 1988) in place of the slope-limited Roe solver. The entrainment process and the complex vortex structure at the mixture–pure fluid interface were identical to those obtained using the Roe solver, and, although the mixture–pure fluid interface was slightly sharper, the results in the sediment region suffered from the same type of errors as in the one-dimensional case (Fig. 4). A third simulation was performed using the first-order finite volume scheme (the Roe solver without the higher-order correction). In this case, the entrainment process was not satisfactorily resolved.

5. Conclusion

Numerical simulations of separating mixture flows at moderate to high Reynolds numbers have been considered. The mixture model was formulated in terms of volume averaged flux densities (velocities) to ensure well-posedness of the incompressibility constraint. A hybrid discretisation scheme for mixture flows in general geometries was presented. Time-splitting and pressure-correction methods were used to achieve faster convergence, by alleviating the CFL condition and decoupling the incompressibility constraint. The spatial discretisation of the momentum and continuity equations was obtained by a Galerkin finite element method combined with an upwind finite difference scheme for the advective terms. A quasi-second-order finite volume scheme based on a slope-limiting procedure was designed to treat conservation of the dispersed phase. The

method employs the finite element grid for its implementation, has no free parameters and requires no additional boundary conditions.

The performance of the various discretisation schemes was demonstrated by considering three fundamental problems from separation technology. The higher robustness of the slope-limited Roe solver over the traditional FEM-FCT method was shown by comparing the results with the analytic solution for one-dimensional gravity settling. Spin-up from rest of a mixture of light particles was studied to validate the numerical treatment of strongly non-linear effects and the resolution of kinematic shocks representing interfaces between mixture and pure-fluid regions. The results were found to be in excellent agreement with previous numerical computations by Amberg and Ungarish (1993). Further verification was given by a comparison between the boundary layer profiles close to the axis of rotation and those obtained from a modified von Kármán formulation. The latter corresponds to the leading order problem of an expansion introduced by Ungarish and Greenspan (1983) for a two-fluid formulation. The next order problem suffers from a mathematical deficiency which makes it impossible to satisfy the no-flux condition at the solid boundary. No such problematic behavior was encountered in the numerical simulation, which seems to indicate that the mixture formulation does not suffer from a similar mathematical deficiency.

A simulation of gravity settling underneath a curved wall was performed for the intermediate parameter regime where both viscous and inertia effects are important. The Boycott layer was observed to form spontaneously in the simulations. Blasius series expansions were derived for the flow in the Boycott layer and in the adjacent mixture region. Although the series converge rapidly, the agreement with numerical results was found to be poor for small angles (see Fig. 9). The reasons for this appear to be the relatively slow growth of the viscous sublayer on the curved wall and a strong influence from the flow in the mixture bulk. Initially, the bulk-flow is accurately described by the kinematic model of Schneider (1982). At later stages, the numerical results reveal a more complicated behavior, beyond the reach of any existing theory. The flux emerging at the top of the Boycott layer is reversed into the interior by a localized vortex and entrains into the mixture bulk. A secondary vortex appears on the horizontal mixture–pure fluid interface and starts to oscillate back and forth between the vertical wall and the primary vortex. The combined effect of entrainment and vortex motion is a stratification of the horizontal interface. As the flow becomes weaker, the interface starts to gradually become sharper due to hindered settling effects. If adjusted for an initial transient (corresponding to the formation of the Boycott layer) and for the finite width of the Boycott layer, PNK theory yields good predictions for the position of the separation front.

In the absence of quantitative concentration and velocity measurements, experimental verification of the results presented herein must be limited to comparison with integral flow scales such as batch separation times and boundary/Boycott layer thicknesses. Since the numerical results were presented together with asymptotic theories for which experimental verification has already been obtained, no direct comparison with experiments is warranted at this time. The computations presented here were performed in axi-symmetric and two-dimensional geometries respectively. Currently, a fully three-dimensional version of the code is being tested. Once up-and-running, this version might be able to resolve some of the presently unattainable issues, such as stability and transition of mixture flows in arbitrary geometries. Further development on both the theoretical and numerical levels is needed for studies involving multi-modal suspensions.

Although some investigations on the rheology of such mixtures have been performed (Shauly et al., 1998; Greenspan and Nigam, 2001), fundamental properties such as adequate semi-empirical expressions for the effective viscosity are still lacking.

Acknowledgements

Professor Harvey P. Greenspan of the Department of Mathematics at MIT is gratefully acknowledged for many fruitful suggestions and comments regarding this work. The research was supported by the Swedish Research Council for Engineering Sciences.

Appendix A

Rate of change of mixture momentum:

$$\frac{\partial}{\partial t}(\phi\rho_{\mathrm{d}}\mathbf{v}_{\mathrm{d}}+(1-\phi)\rho_{\mathrm{C}}\mathbf{v}_{\mathrm{C}})=\rho_{\mathrm{C}}\frac{\partial}{\partial t}((1+\varepsilon)\mathbf{j}_{\mathrm{d}}+\mathbf{j}_{\mathrm{C}})=\rho_{\mathrm{C}}\left(\frac{\partial\mathbf{j}}{\partial t}+\varepsilon\frac{\partial\mathbf{j}_{\mathrm{d}}}{\partial t}\right).$$

Mixture momentum flux:

$$\begin{aligned}\phi\rho_{\mathrm{d}}\mathbf{v}_{\mathrm{d}}\mathbf{v}_{\mathrm{d}}+(1-\phi)\rho_{\mathrm{C}}\mathbf{v}_{\mathrm{C}}\mathbf{v}_{\mathrm{C}}&=\rho_{\mathrm{C}}\left(\frac{(1+\varepsilon)\mathbf{j}_{\mathrm{d}}\mathbf{j}_{\mathrm{d}}}{\phi}+\frac{\mathbf{j}_{\mathrm{C}}\mathbf{j}_{\mathrm{C}}}{1-\phi}\right)=\rho_{\mathrm{C}}\left(\frac{(1+\varepsilon)\mathbf{j}_{\mathrm{d}}\mathbf{j}_{\mathrm{d}}}{\phi}+\frac{(\mathbf{j}-\mathbf{j}_{\mathrm{d}})(\mathbf{j}-\mathbf{j}_{\mathrm{d}})}{1-\phi}\right)\\&=\rho_{\mathrm{C}}\left(\frac{(1+\varepsilon)\mathbf{j}_{\mathrm{d}}\mathbf{j}_{\mathrm{d}}}{\phi}+\frac{\mathbf{j}\mathbf{j}-\mathbf{j}_{\mathrm{d}}\mathbf{j}-\mathbf{j}\mathbf{j}_{\mathrm{d}}+\mathbf{j}_{\mathrm{d}}\mathbf{j}_{\mathrm{d}}}{1-\phi}\right)\\&=\rho_{\mathrm{C}}\left(\frac{(1-\phi)(1+\varepsilon)\mathbf{j}_{\mathrm{d}}\mathbf{j}_{\mathrm{d}}+\phi\mathbf{j}\mathbf{j}-\phi(\mathbf{j}_{\mathrm{R}}+\phi\mathbf{j})\mathbf{j}-(\mathbf{j}_{\mathrm{d}}-\mathbf{j}_{\mathrm{R}})\mathbf{j}_{\mathrm{d}}+\phi\mathbf{j}_{\mathrm{d}}\mathbf{j}_{\mathrm{d}}}{\phi(1-\phi)}\right)\\&=\rho_{\mathrm{C}}\left(\frac{\varepsilon(1-\phi)\mathbf{j}_{\mathrm{d}}\mathbf{j}_{\mathrm{d}}+\phi(1-\phi)\mathbf{j}\mathbf{j}+\mathbf{j}_{\mathrm{R}}(\mathbf{j}_{\mathrm{d}}-\phi\mathbf{j})}{\phi(1-\phi)}\right)\\&=\rho_{\mathrm{C}}\left(\frac{\varepsilon\mathbf{j}_{\mathrm{d}}\mathbf{j}_{\mathrm{d}}}{\phi}+\mathbf{j}\mathbf{j}+\frac{\mathbf{j}_{\mathrm{R}}\mathbf{j}_{\mathrm{R}}}{\phi(1-\phi)}\right).\end{aligned}$$

The stationary shock-conditions to be satisfied at a concentration discontinuity are given by,

$$[\mathbf{j}]_{-}^{+}=\mathbf{0},$$

$$[\hat{\boldsymbol{n}}\cdot\mathbf{j}_{\mathrm{d}}]_{-}^{+}=0,$$

$$\left[\hat{\boldsymbol{n}}\cdot\left(\mathbf{j}\mathbf{j}+\frac{\mathbf{j}_{\mathrm{R}}\mathbf{j}_{\mathrm{R}}}{\phi(1-\phi)}+\frac{\varepsilon\mathbf{j}_{\mathrm{d}}\mathbf{j}_{\mathrm{d}}}{\phi}\right)\cdot\hat{\boldsymbol{n}}\right]_{-}^{+}=\frac{1}{\rho_{\mathrm{C}}}\left[\hat{\boldsymbol{n}}\cdot\underline{\underline{\Sigma}}\cdot\hat{\boldsymbol{n}}\right]_{-}^{+},$$

$$\left[\hat{\boldsymbol{n}}\times\left(\mathbf{j}\mathbf{j}+\frac{\mathbf{j}_{\mathrm{R}}\mathbf{j}_{\mathrm{R}}}{\phi(1-\phi)}+\frac{\varepsilon\mathbf{j}_{\mathrm{d}}\mathbf{j}_{\mathrm{d}}}{\phi}\right)\cdot\hat{\boldsymbol{n}}\right]_{-}^{+}=\frac{1}{\rho_{\mathrm{C}}}\left[\hat{\boldsymbol{n}}\times\underline{\underline{\Sigma}}\cdot\hat{\boldsymbol{n}}\right]_{-}^{+},$$

where $\hat{\boldsymbol{n}}$ is the local unit-normal at the interface. These conditions express continuity of mixture velocity, normal particle flux and mixture momentum across the interface.

Appendix B

Interpolation coefficients:

$$\varphi(t) = \left[\frac{(t-t^n)^2 + 3\,\Delta t(t-t^n) + 2\,\Delta t^2}{2\,\Delta t^2}\right]\varphi^n - \left[\frac{(t-t^n)^2 + 2\,\Delta t(t-t^n)}{\Delta t^2}\right]\varphi^{n-1} + \left[\frac{(t-t^n)^2 + \Delta t(t-t^n)}{2\,\Delta t^2}\right]\varphi^{n-2} + \mathrm{O}(\Delta t^3) \quad \text{for } t^{n-1} < t < t^{n+1},$$

$$\frac{\partial\varphi}{\partial t} = \left[\frac{2(t-t^n) + 3\,\Delta t}{2\,\Delta t^2}\right]\varphi^n - \left[\frac{2(t-t^n+\Delta t)}{\Delta t^2}\right]\varphi^{n-1} + \left[\frac{2(t-t^n) + \Delta t}{2\,\Delta t^2}\right]\varphi^{n-2} + \mathrm{O}(\Delta t^2) \quad \text{for } t^{n-1} < t < t^{n+1}.$$

Appendix C

The finite element bases for X_h^{v} and X_h^{p} are defined by partitioning the computational domain $\mathscr{R}$ into K non-overlapping triangular elements, $\mathscr{R} = \cup_{k=1}^{K}\mathscr{R}^k$, and representing functions within each element as tensor-product polynomials on a reference element $\hat{\mathscr{R}}$ defined as the isosceles triangle with vertices at (0,0), (1,0) and (0,1). The subspaces used in the finite element discretisations are

$$X_h^{\mathrm{v}} = X_h^{\mathrm{p}} = \{v|_{\mathscr{R}^k} \in \mathbb{P}^1(\mathscr{R}^k)\} \cap \mathscr{H}^1(\mathscr{R}),$$

$$X_{h0}^{\mathrm{v}} = \{v|_{\mathscr{R}^k} \in \mathbb{P}^1(\mathscr{R}^k)\} \cap \mathscr{H}_0^1(\mathscr{R}),$$

where subscript 0 refers to homogeneous Dirichlet conditions. $\mathbb{P}^1$ is the set of tensor-product polynomials of degree 1 and $\mathscr{H}^1$ is the space of all square integrable functions on $\mathscr{R}$ whose first derivatives are also square integrable. The discrete counterpart to (31)–(35) is given by,

$$\left(\frac{3}{2\,\Delta t}\mathscr{M} + v_0\mathscr{A}^n\right)\underline{\mathbf{j}}_{h0}^{*} = \frac{1}{\rho_{\mathrm{C}}}\mathscr{D}^{\mathrm{T}}\underline{p}_h^{n-1} + \mathscr{M}\underline{\mathbf{f}}_{h\mathrm{b}}^{n},$$

$$\frac{2\,\Delta t}{3\rho_{\mathrm{C}}}A_{pp}\,\underline{\delta p}_h = \mathscr{D}\underline{\mathbf{j}}_{h0}^{n} - \mathscr{D}\underline{\mathbf{j}}_{h0}^{*},$$

$$-\mathscr{D}\underline{\mathbf{j}}_{h0}^{n} = \underline{g}_h^{n},$$

$$\mathscr{M}\underline{\mathbf{j}}_{h0}^{n} = \mathscr{M}\underline{\mathbf{j}}_{h0}^{*} + \frac{2\,\Delta t}{3\rho_{\mathrm{C}}}\mathscr{D}^{\mathrm{T}}\,\underline{\delta p}_h,$$

$$\underline{p}_h^{n} = \underline{p}_h^{n-1} + \underline{\delta p}_h,$$

where superscript n on $\mathscr{A}^n$ refers to the dependence on $\underline{\phi}_h^n$ and the tensors have the following shapes:

$$\mathscr{M} = \begin{bmatrix} M & 0 & 0 \\ 0 & M & 0 \\ 0 & 0 & M \end{bmatrix},$$

$$\mathscr{A}^n = \begin{bmatrix} A_{11}^n & A_{12}^n & A_{13}^n \\ (A_{12}^n)^{\mathrm{T}} & A_{22}^n & A_{23}^n \\ (A_{13}^n)^{\mathrm{T}} & (A_{23}^n)^{\mathrm{T}} & A_{33}^n \end{bmatrix},$$

$$\mathscr{D} = [D_1 \quad D_2 \quad D_3],$$

$$\underline{\mathbf{j}}_{h0}^{n,*} = \left[\underline{j}_{h01}^{n,*} \quad \underline{j}_{h02}^{n,*} \quad \underline{j}_{h03}^{n,*}\right]^{\mathrm{T}},$$

$$\underline{\mathbf{f}}_{h\mathrm{b}}^{n} = \left[\underline{\mathrm{f}}_{h\mathrm{b}1}^{n} \quad \underline{f}_{h\mathrm{b}2}^{n} \quad \underline{f}_{h\mathrm{b}3}^{n}\right]^{\mathrm{T}}.$$

The projection error is obtained by eliminating $\underline{\mathbf{j}}_{h0}^{*}$,

$$\left(\frac{3}{2\Delta t}\mathscr{M} + v_0\mathscr{A}^n\right)\underline{\mathbf{j}}_{h0}^{n} - \frac{1}{\rho_{\mathrm{C}}}\mathscr{D}^{\mathrm{T}}\underline{p}_h^n - \mathscr{M}\underline{\mathbf{f}}_{h\mathrm{b}}^{n} = \frac{2v_0\Delta t}{3\rho_{\mathrm{C}}}\mathscr{A}^n\mathscr{M}^{-1}\mathscr{D}^{\mathrm{T}}\underline{\delta p}_h.$$

Since $\underline{\delta p}_h$ is $\mathrm{O}(\Delta t)$, the method is $\mathrm{O}(\Delta t^2)$.

References

Acrivos, A., Herbolzheimer, E., 1979. Enhanced sedimentation in settling tanks with inclined walls. J. Fluid Mech. 92, 455–457.

Amberg, G., Ungarish, M., 1993. Spin-up from rest of a mixture: numerical simulation and asymptotic theory. J. Fluid Mech. 246, 443–464.

Courant, R., Friedrichs, K., Lewy, H., 1967. On the partial difference equations of mathematical physics IBM. J. Res. Develop. 11, 215–234.

Fletcher, C.A.J., 1983. The group finite-element formulation. Comput. Methods Appl. Mech. Eng. 37, 225–244.

Greenspan, H.P., 1983. On centrifugal separation of a mixture. J. Fluid Mech. 127, 91–101.

Greenspan, H.P., Nigam, M.S., 2001. A note on separation of a bimodal mixture in pipe flow. Int. J. Multiphase Flow 27, 2015–2021.

Greenspan, H.P., Ungarish, M., 1985. On the centrifugal separation of a bulk mixture. Int. J. Multiphase Flow 11, 825–835.

Hill, W.D., Rothfus, R.R., Kun, L., 1977. Boundary-enhanced sedimentation due to settling convection. Int. J. Multiphase Flow 3, 561–583.

Holmqvist, C., 1998. Sedimentation in a container with a cylindrically curved wall. TRITA-MEK, Technical Report 1998:3, ISSN 0348-467X, ISRN KTH/MEK/TR-98/3-SE, vol. 127, pp. 263–281.

Hyun, J.M., Leslie, F., Fowlis, W.W., 1983. Numerical solutions for spin-up from rest in a cylinder. J. Fluid Mech. 127, 263–281.

Jana, S.C., Kapoor, B., Acrivos, A., 1995. Apparent wall slip velocity coefficients in concentrated suspensions of noncolloidal particles. J. Rheol. 39, 1123–1132.

Krieger, I.M., 1972. Rheology of monodisperse latices. Adv. Colloid. Interface Sci. 3, 111–136.

Kynch, G.J., 1952. A theory of sedimentation. Trans. Faraday Soc. 48, 166–176.

LeVeque, R.J., 1990. Numerical Methods for Conservation Laws. Birkhäuser-Verlag.

Löhner, R., 1988. FEM-FCT-combining unstructured grids with high-resolution. Commun. Appl. Numer. Meth. 4, 717–729.

Maday, Y., Patera, A.T., Rønquist, E.M., 1990. An operator-integration-factor splitting method for time-dependent problems: Application to incompressible fluid flow. J. Sci. Comput. 5, 310–337.

Nakamura, H., Kuroda, K., 1937. La cause de l'accélération de la vitesse de sédimentation des suspensions dans les récipients inclinés. Keijo J. Med. 8, 256–296.
Peyrard, P.F., Villedieu, P., 1998. A Roe scheme for ideal MHD equations on 2D adaptively refined triangular grids. J. Comput. Phys. 150, 373–393.
Phillips, R.J., Armstrong, R.C., Brown, R.A., 1992. A constitutive equation for concentrated suspensions that accounts for shear-induced particle migration. Phys. Fluids A 4, 30–40.
Ponder, E., 1925. On sedimentation and roleaux formation. Quart. J. Exp. Physiol. 15, 235–252.
Schaflinger, U., 1997. Hydrodynamic diffusion of sedimenting non-Brownian particles: experimental observations. Technische Universität Wien, Internal Report.
Schneider, W., 1982. Kinematic-wave theory of sedimentation beneath inclined walls. J. Fluid Mech. 120, 323–346.
Shaqfeh, E.S.G., Acrivos, A., 1986. The effects of inertia on the buoyancy-driven convection flow in settling vessels having inclined walls. Phys. Fluids. 29, 3935–3948.
Shauly, A., Wachs, A., Nir, A., 1998. Shear-induced particle migration in a polydisperse concentrated suspension. J. Rheol. 42, 1329–1348.
Strang, G., Fix, G., 1973. An Analysis of the Finite Element Method. Prentice-Hall.
Subia, S.R., Ingber, M.S., Mondy, L.A., Altobelli, S.A., Graham, A.L., 1998. Modelling of concentrated suspensions using a continuum constitutive equation. J. Fluid Mech. 373, 193–219.
Tabata, M., Fujima, S., 1991. An upwind finite element scheme for high Reynolds number flows. Int. J. Numer. Meth. Fluids 12, 305–322.
Ungarish, M., 1991. Spin-up from rest of a light particle suspension in a cylinder: theory and observations. Int. J. Multiphase Flow 17, 131–143.
Ungarish, M., 1993. Hydrodynamics of Suspensions. Springer-Verlag.
Ungarish, M., Greenspan, H.P., 1983. On two-phase flow in a rotating boundary layer. Stud. Appl. Math. 69, 145–175.
Venezian, G., 1970. Nonlinear spin-up. Top. Ocean Eng. 2, 87–96.